Experimental investigation of non-normality of thermoacoustic interaction in an electrically heated Rijke tube

Sathesh Mariappan[*, 1]**, R. I. Sujith**[†, 1] **and Peter J. Schmid**[‡, 2]

[1]*Department of Aerospace Engineering, Indian Institute of Technology Madras*
Chennai 600036, India

[2]*Department of Mathematics, Imperial College London, SW7 2AZ, UK*

ABSTRACT

An experimental investigation of the non-normal nature of thermoacoustic interactions in an electrically heated horizontal Rijke tube is performed. Since non-normality and the associated transient growth are linear phenomena, the experiments have to be confined to the linear regime. The bifurcation diagram for the subcritical Hopf bifurcation into a limit cycle behavior has been determined, after which the amplitude levels, for which the system acts linearly, have been identified for different power inputs to the heater. There are two main objectives for this experimental investigation. The first one deals with the extraction of the linear eigenmodes associated with the acoustic pressure from experimental data. This is accomplished by the Dynamic Mode Decomposition (DMD) technique applied in the linear regime. The non-orthogonality between the eigenmodes is determined for various values of heater power. The second objective is to identify evidence of transient perturbation growth in the system. The total acoustic energy in the duct has been monitored as the thermoacoustic system evolves from its initial condition. Transient growth, on the order of previous theoretical studies, has been found, and its parameteric dependence on amplitude ratio and phase angle of the initial eigenmode components has been determined. This study represents the first experimental confirmation of non-normality in thermoacoustic systems.

1. INTRODUCTION

Thermoacoustic instabilities are a common feature in many combustion systems. They arise, for example, when acoustic oscillations in a combustion chamber are amplified via a positive feedback of unsteady heat release rates stemming from the heat source in the chamber. Even though the details and characteristics of thermoacoustic instabilities

---

[*]Corresponding author: sathesh.ae@gmail.com, Currently, Assistant Professor, Department of Aerospace Engineering, Indian Institute of Technology Kanpur, Kanpur 208016, India

[†]Professor, Author to whom correspondence should be addressed: sujith@iitm.ac.in

[‡]Professor

depend on the particularities of the physical and geometric setup, a great deal of insight into the fundamental mechanisms underlying these instabilities can be gained from a study of a simple model problem: the Rijke tube — an elementary thermoacoustic device that contains much of the essential physics of thermoacoustic interactions.

Due to its simplicity and representative character, the study of thermoacoustic instabilities in a Rijke tube has a long history, going back to the original investigation of Rijke [1] who observed acoustic amplifications in a vertical tube as a coiled electrical heating filament is turned on. Over the past decades, this observation has given rise to a significant body of literature exploring this phenomenon by numerical simulations [2, 3, 4, 5, 6] or by experimental efforts [7, 8]. The goal of these studies was a better understanding of the basic mechanisms linking the acoustic field in the chamber to the unsteady heat release rates.

Recently, thermoacoustic systems have been shown to be non-normal [9, 10]. The resulting non-orthogonality of the eigenmodes of the linearized operator leads to transient growth of oscillations for an appropriate set of initial conditions, even for parameter combinations for which the system is linearly stable. The non-normality warrants an investigation of the short-term behavior of thermoacoustic systems [11, 12] which has been accomplished numerically for instabilities in a ducted diffusion flame [9], in a Rijke tube [10] and in solid-rocket motors. Nonlinear effects and corresponding optimal initial conditions have been treated by Juniper [13] using a nonlinear adjoint optimization technique; their role in the asymptotic (long-term) stability of the system has also been determined. Furthermore, the effect of noise on the stability of thermoacoustic oscillations in a Rijke tube has been explored numerically [14, 15]. They observed that pink noise (higher noise amplitudes in the lower frequency range) is effective in causing the system to become unstable and postulated that this is because the initial state that causes triggering from lowest energy (the 'most dangerous initial state') also has higher amplitudes in the low frequency range.

The concept of transient growth first arose in the stability analysis of shear flows [16], where the essential role of short-term energy amplification based on a linear process has been established by theoretical calculations and numerical simulations [17, 18]. Substantially fewer studies have been experimental. The earliest experimental results have been reported by Mayer & Reshotko [19], who observed transient growth of disturbance amplitudes in a pipe flow experiment. The formation of streaky structures (i.e., streamwise elongated regions of high and low velocities) in boundary layers, which can be attributed to the non-normal nature of the linearized system, is another example of experimental evidence for transient growth [20]. In the same experimental configuration, stable laminar streaks have been generated and transient spatial amplitude growth has been observed in the streamwise direction [21]. Furthermore, passive control of transition to turbulence in a boundary layer has been attempted by exploiting the non-normal nature of the system [22].

The experimental confirmation of theoretical and numerical observations gives greater weight to the role of non-normal effects in wall-bounded shear flows and establishes this concept as a valid component in transitional shear flows. The same confirmation for thermoacoustic systems is as yet missing; but the present study is

intended to fill this gap. In particular, we will identify the non-normal nature of thermoacoustic interactions in a Rijke tube experimentally and quantify the amount of transient energy growth in acoustic energy it yields. To this end, the present paper focusses on two main issues. The first one is concerned with the experimental extraction of eigenmodes from the Rijke tube which is accomplished by the Dynamic Mode Decomposition (DMD) introduced in Schmid [23]. This is followed by confirming the non-orthogonality of the extracted eigenmodes. The second issue deals with the quantification of transient growth, measured in the acoustic energy, by generating specific initial conditions with an acoustic driver.

The remaining paper is structured as follows: the experimental configuration of the Rijke tube system is described in section 2, after which the employed experimental procedures (section 3) and their theoretical background are introduced. These tools will then be employed on the Rijke tube experiment and the obtained results will be discussed in light of the two main issues of this inquiry (section 4.3 and section 4.4). Concluding remarks will be given in section 5.

2. EXPERIMENTAL CONFIGURATION OF THE RIJKE TUBE

The experimental setup consists of a $1m$ long Rijke tube made of aluminium. The tube has a square cross section, with an area of $92 \times 92 \ mm^2$. A schematic diagram of the experimental configuration is shown in figure 1. A mean flow is established in the tube, using a blower operated in suction mode, and the volume flow rate is measured by a
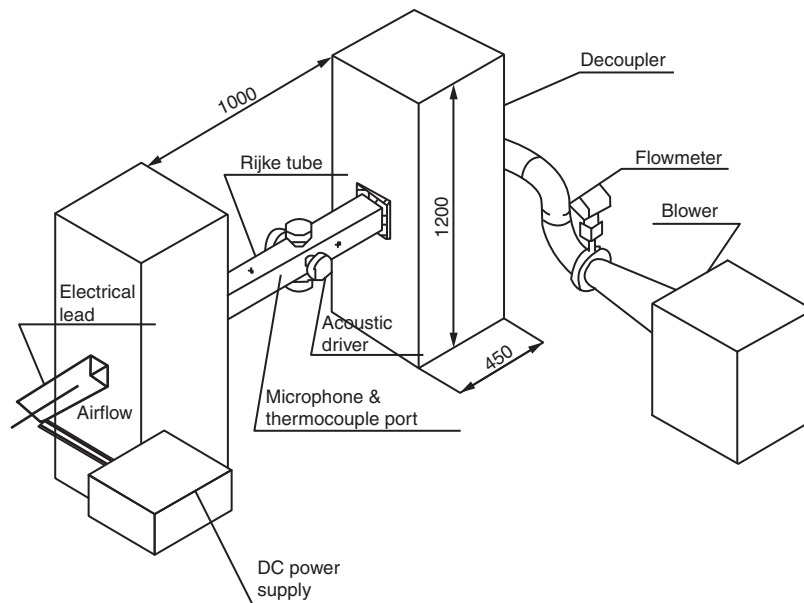

Figure 1:   Schematic diagram of the Rijke tube experiment. All dimensions are given in mm.
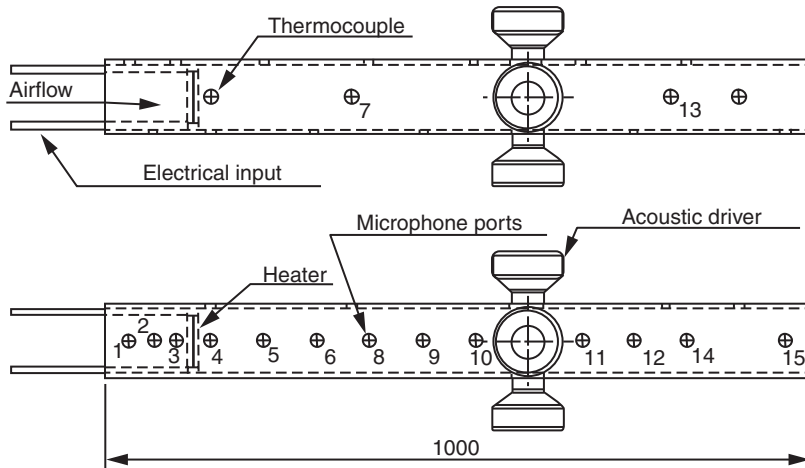
Figure 2:   Configuration of the Rijke tube showing the heater, the microphone ports and the acoustic drivers. The locations of the microphone ports are numbered, and their distances from the upstream edge of the tube are listed in table 1. All dimensions are given in mm.

compact-orifice mass-flow meter (Rosemount 3051 SFC) located just upstream of the blower. The measurement range of the flow meter is $0-5$ g/s with an uncertainty of $\pm 2.1\%$ of the mass flow rate. Two decouplers ($120 \times 45 \times 45$ cm^3) — one upstream, one downstream of the tube — are located so as to provide acoustic open-open boundary conditions.

Details of the Rijke tube are shown schematically in figure 2. A mesh-type (size 30) electrical heater can be located at any desired axial location, and a programmable DC power supply (TDK-Lambda, GEN8-400, $0-8\,V$, $0-400A$) is used to power the electrical heater. The horizontal Rijke tube configuration described in this paper is similar to the one reported [7, 8]. Two thermocouples have been installed, one at the inlet of the tube and the other downstream of the heater; these are used to monitor the steady state temperature in the duct. Four acoustic driver units (Ahuja AU 60) are mounted on the walls of the tube to impose a prescribed acoustic initial condition on the system. A total of 15 microphones are placed along the duct in order to record the evolution of acoustic pressure. The microphones are distributed such that the first two eigenmodes of the system can be determined efficiently. The precise locations of the heater, the thermocouples, the acoustic drivers and the microphones are schematically displayed in figure 2 and tabulated in table 1. Data are acquired simultaneously using the programmable National Instruments PCI 6221 & 6251 data acquisition cards at 8 kHz.

Table 1: The locations of the microphones, heater, thermocouple and loudspeakers, measured from the upstream edge of the Rijke tube.

Microphone no.	Location (mm)	Microphone no.	Location (mm)
1	35	10	675
2	70	11	750
3	100	12	800
4	150	13	825
5	225	14	900
6	300	15	965
7	375	Heater	125
8	450	Thermocouple	150
9	525	Acoustic driver unit	600

3. EXPERIMENTAL PROCEDURES AND THEORETICAL BACKGROUND

The non-normal nature of our system results in non-orthogonal eigenmodes which, in turn, can lead to transient growth of the thermoacoustic oscillations. Transient growth is a linear phenomenon and any experimental analysis of this phenomenon has to ensure operation in the linear regime (a more precise definition will be given in section 3.2). An attempt is then made to determine the non-orthogonality between the first two eigenmodes of the system and to experimentally observe and quantify transient growth associated with these two modes. For the extraction of the eigenmodes, the Dynamic Mode Decomposition (DMD) technique [23] will be used which yields eigenmodes of the system as long as the experiment is performed in the linear regime. In the following subsections, we introduce tools, techniques and experimental procedures, such as bifurcation analysis (section 3.1), linear regime detection (section 3.2), extraction of acoustic dynamic modes (section 3.3) and validation of the technique (section 3.4 and section 3.5) and experimental exploration of transient growth potential (section 3.6), before these methods will be applied to measurements from our experiments (in section 4).

3.1. Bifurcation diagram

In a first step, the bifurcation behavior of the full, nonlinear system is obtained which will guide us in the parameter space, establish various stability limits and, in particular, determine the regions where a (predominantly) linear behavior can be expected or assumed. A bifurcation diagram consists of a relation between a pertinent control parameter and the asymptotic state of the system (properly parameterized by a specified, representative variable, such as, e.g., the energy or disturbance amplitude). As the power supplied to the heater (our control parameter) is increased, it has been observed in earlier investigations [24, 8] that the transition to instability occurs via a subcritical Hopf bifurcation. The subcritical nature of the bifurcation allows the co-existence of a stable

fixed point and a limit cycle, and this particular parameter regime is also referred to as the *bistable region* [4]. In this region, the system is linearly stable but can nevertheless be forced into a limit cycle, if the initial condition falls above some threshold amplitude. The minimum amplitude that ultimately yields a limit-cycle behavior is known as the triggering amplitude of the system, and specific experimental details of its determination are given in section 4.1. The obtained triggering amplitudes provide an estimate of the acoustic pressure amplitudes at which nonlinear effects play a significant role in the qualitative behavioral change (limit cycle or fixed point) of the system.

3.2. Regime of linear behavior

A linear system can be defined as one in which, when the amplitude of the input is scaled by a given amount, the amplitude of the output is scaled by the same amount. In the present case, the input variable is the voltage supplied to the acoustic drivers, while the output variable is the acoustic pressure measured at a given location in the tube. For a user-specificied heater power, the above input is varied and the output is recorded; the response curve of the system can thereby be obtained. For our purposes, the limit of linearity is reached when the deviation of the system's response from the linearized response function (see Appendix A for details) exceeds 5% of the corresponding triggering amplitude. The experiments probing the non-normal nature of our thermoacoustic system are performed with amplitude levels below the limit of linearity. The selected number 5% is an arbitrary cut off. The cutoff determines the limit of linearity, which needs to be large enough, so that acoustic pressure measurements can be performed with a high signal to noise ratio. On the other hand, the same number is not chosen very large, so that the effects of nonlinearities are significant.

3.3. Dynamic mode decomposition

In pursuit of the first goal of the present investigation, the acoustic eigenmodes of the system have to be extracted. This can be accomplished, for example, by using network models for each acoustic component [25] where each individual acoustic elements is described by a transfer matrix, which can be determined experimentally [25] or numerically [26]. The eigenfrequencies and corresponding eigenmodes of the system can then be calculated from the assembled network matrix. The transfer matrices associated with the flame elements are obtained by forcing the flame continuously, and measuring its response experimentally. The required experiment has to be performed at low amplitudes of forcing, where the system behaves linearly, and the accurate identification of the transfer matrices in this regime may prove difficult [27]. In addition, the acoustic fields upstream and downstream of the heat source have to be modeled as separate acoustic elements, making this process rather time consuming. Due to its composite nature, any error in the calculation of any one of the transfer matrices will propagate and reflect on the final result. Finally, the transfer matrix technique has been developed for a frequency-domain analysis; extending it to the time-domain is nontrivial. To circumvent the above issues, we choose to extract the eigenmodes via a Dynamic Mode Decomposition [23] which isolates the modes from a time series of acoustic pressure measurements simultaneously acquired at various locations on the Rijke tube.

Dynamic Mode Decomposition (DMD) is a data-based technique that extracts dominant dynamic features from a time-resolved sequence of flow field measurements. The identified dominant flow structures are termed *dynamic modes*; data from numerical simulations and experiments can be processed. When the flow process, from which the snapshots are sampled, is linear, the application of DMD is equivalent to a global stability analysis [28], and the dynamic modes thus obtained are the eigenmodes of the system. This technique has been applied to a variety of flow configurations, such as flow in a lid driven cylindrical cavity [29] using time-resolved particle-image velocimetry (PIV) measurements in a cross-sectional plane, flow of a helium jet [30] using Schlieren images as snapshots, or numerical simulations of a jet flame and experiments for a water jet [31]. In all cases, the dominant frequencies and the associated flow structures could be detected. Furthermore, DMD was recently applied to both experimental [32] and numerical [32, 6] data to analyze thermoacoustic interactions.

In the present investigation, experiments are performed in the linear regime to extract the first two eigenmodes of the system. The Rijke tube system is initially perturbed using acoustic driver units in a manner that excites the dominant eigenmodes of the system. The temporal evolution of the acoustic pressure is recorded by microphones, after which the DMD technique is applied to the acquired data. The first two acoustic pressure eigenmodes of the system are then isolated from the DMD spectrum. After obtaining the eigenmodes of the system, their mutual non-orthogonality is quantified by computing the inner product $\langle p_i, p_j \rangle = \int_0^L p_i^* p_j dx$, where p_i represents the ith eigenmode of the system, properly normalized according to $\langle p_i, p_i \rangle = 1$. The length of the tube is denoted by L, and the superscript $*$ stands for the complex conjugate. The above definition of the inner product is identical to the one used by Culick [33] and Nicoud *et al*. [34]. The inner product is calculated for various values of heater power levels; the results are presented and discussed in section 4.3.

3.4. Theoretical investigation of the eigenmodes

To gain more confidence in the results, DMD is first applied to the synthetic data. We generate synthetic data from a theoretical model, extract the eigenvalues and eigenmodes using DMD and compare them to the theoretical results. Thermoacoustic interactions in the Rijke tube system can be represented by the following linearized acoustic momentum and energy equations, given in nondimensionalized form [10],

$$\frac{\partial u}{\partial t} + \frac{\partial p}{\partial x} = 0, \tag{1a}$$

$$\frac{\partial p}{\partial t} + \frac{\partial u}{\partial x} = Q\delta\left(x - x_f\right), \tag{1b}$$

where, u and p are the nondimensionalized acoustic velocity and pressure, respectively, Q is the nondimensionalized unsteady heat release rate and x_f is the location of the heat

source in the tube. The effect of steady-state flow and temperature gradients in the duct are neglected. The heat source is assumed to be compact compared to the length of the tube and is thus represented by a Dirac-delta function ($\delta(x)$). The jump conditions across the heater are as follows [35]:

$$p(x_f^+, t) = p(x_f^-, t) \tag{2a}$$

$$u(x_f^+, t) - u(x_f^-, t) = Q(t) \tag{2b}$$

where the superscript $\pm$ indicates the value of the variables upstream or downstream of the heat source. The unsteady heat release rate from the heat source is modeled using the common $n - \tau$ model [36] and is of the form

$$Q = nu(x_f^-, t - \tau) \tag{3}$$

with n as the interaction index, which indicates the power supplied to the heater, and τ as the time lag associated with the acoustic velocity fluctuations upstream of the heat source. The Rijke tube is assumed open at both ends. The eigenmodes of the system are then obtained from the above equations (1-3). The eigenmodes ($\hat{p}$) corresponding to the acoustic pressure of the system, defined in the form $p(x, t) = \hat{p}(x)e^{\omega t}$, are given by

$$\hat{p}(x) = \begin{cases} \sinh\left(\omega x\right), & 0 \leq x \leq x_f, \\ \sinh\left(\omega(x-1)\right)\dfrac{\sinh\left(\omega x_f\right)}{\sinh\left(\omega\left(x_f - 1\right)\right)}, & x_f < x \leq 1, \end{cases} \tag{4}$$

and the corresponding eigenvalues ω satisfy the transcendental dispersion relation

$$\sinh\left(\omega\right) - \frac{n}{2}e^{-\omega\tau}\sinh\left(\omega\left(2x_f - 1\right)\right) = 0. \tag{5}$$

The theoretical pressure eigenmodes of the above system are shown in the left column of figure 3. The heater is located at $x = 0.125$, where the first two eigenmodes of the system becomes less stable [7]. The eigenmodes are numbered as $p_1, p_2, \ldots$, in ascending order of the imaginary part (frequency) of the associated eigenvalues $\omega_1, \omega_2, \ldots$. Each plot contains the real and imaginary part of the first two eigenmodes. When the heater is switched off ($n = 0$), the eigenmodes coincide with the natural duct modes. As the value of n is increased, the eigenmodes progressively deviate from the natural duct modes. A discontinuity in the slope of the eigenmodes is clearly visible at the location of the heat source, a consequence of the acoustically compact nature of the heat source. This change in slope becomes more pronounced as the value of n increases, with a more marked discontinuity in the imaginary part than in the real part. For each subfigure, the value of the nondimensionalized heater power n as well as the degree of non-orthogonality given

by the inner product $|\langle p_1, p_2 \rangle|$ (as described in section 3.3) are displayed in the title. In cold flow ($n = 0$), the eigenmodes of the system (shown in figure 3a) are a simple sine function for the real part and zero for the imaginary part. The inner product $\langle p_1, p_2 \rangle$ is very small, indicating that the eigenmodes are orthogonal in this case. As the value of n is increased, the imaginary part of the respective eigenmodes becomes non-zero; the eigenmodes become increasingly non-orthogonal (see figures 3a, c, e, g). This non-orthogonality between the eigenmodes is caused by the discontinuity in the slope at the location of the heater; the value of the discontinuity, and thus the degree of non-normality, is proportional to n. The above theoretical findings motivate the placement of three microphones on the upstream side of the heater and the remaining twelve microphones downstream of the heater (see table 1), which should facilitate the detection of the modal shapes from the data acquired from the microphone array.

3.5. Extraction of dynamic modes

Data produced by the theoretical model (1) will now be used as input for DMD analysis, and we extract the acoustic pressure data at locations identical to the microphone positions in the experiment (see table 1). A total of 700 snapshots, equispaced in time with a nondimensionalized time-interval of 0.025, have been used.

As only acoustic pressure is measured along the length of the duct and no direct measurements related to the heat source dynamics is taken into account, any dynamic information about the heat source is lost. It is advisable then to apply DMD separately to data from the upstream and the downstream side of the heater. The resulting dynamic
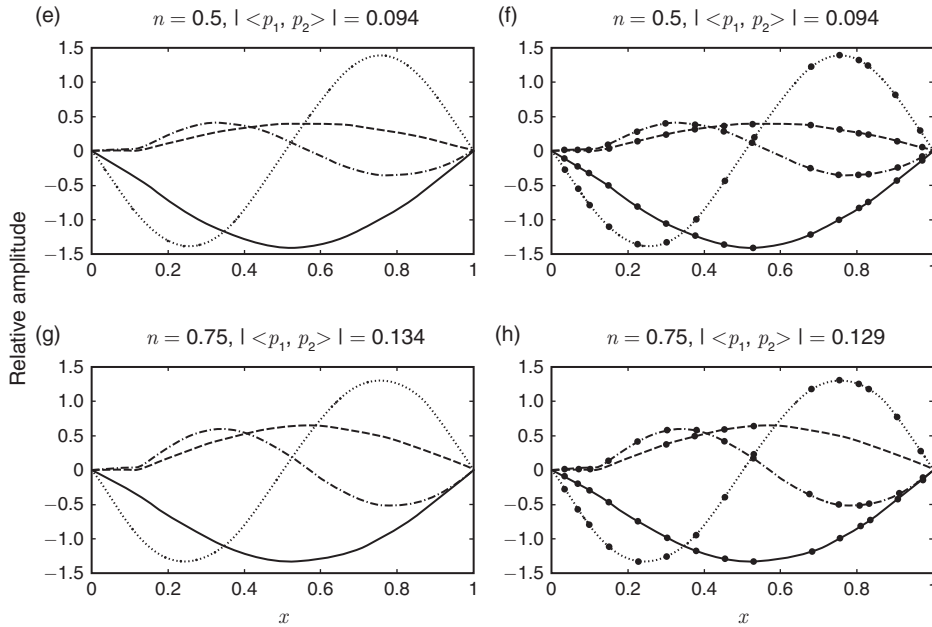

Figure 3 (Continued)
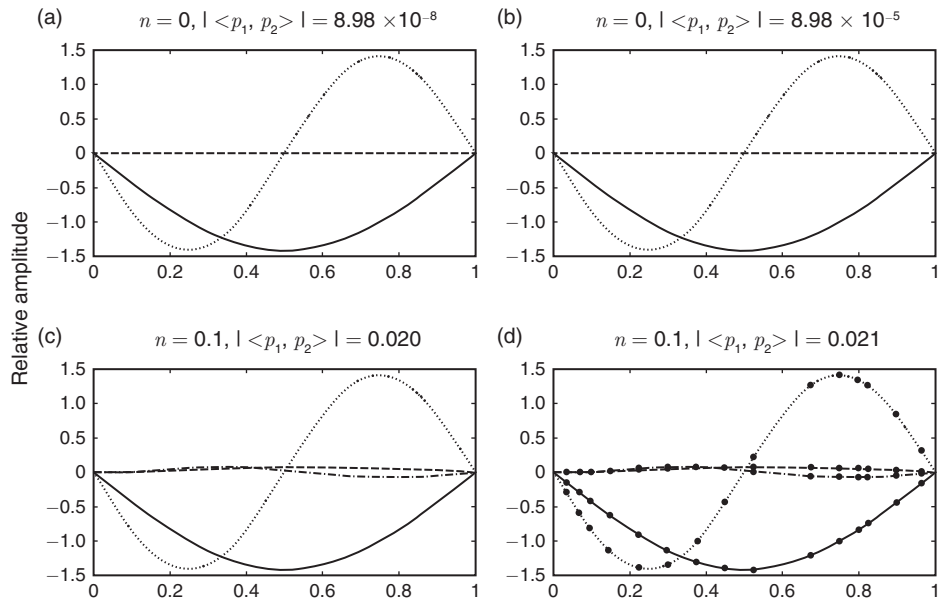
Figure 3:   Comparison of the first two eigenmodes obtained analytically (see (4)) from the $n - \tau$ model (left column) with the eigenmodes obtained by performing DMD on the data obtained from the same model (right column). The value of the nondimensionalized heater power n and the absolute value of the inner product $\langle p_1, p_2 \rangle$ are indicated in the title of each subfigures. The eigenmodes are displayed following the scheme: '——' real part of first eigenmmode, '⋯⋯⋯' real part of second eigenmode, '– – –' imaginary part of first eigenmode, '· – · – ·' imaginary of second eigenmode. The governing parameters are $x_f = 0.125$ and $\tau = 0.2$ (prescribed by Lighthill [37]).

modes are suitably scaled so as to match the acoustic pressure on either side of the heater (see equation 2a).

   For the extraction of the first eigenmode of the system, the model equations (1) evolved forward in time, starting at $t = 0$ with the analytical shape of the first eigenmode. The resulting data set, again separated into upstream and downstream of the heater location, are then processed by the DMD algorithm. The eigenvalues obtained from data of the upstream (symbol '×') and downstream (symbol '∘') side of the heater are shown in figure 4a, for a parameter setting of $n = 0.5$, $x_f = 0.125$ and $\tau = 0.2$. Two dominant, complex conjugate eigenvalues, close to the imaginary axis, are identified together with spurious eigenvalues displaying high frequencies and large decay rates; figure 4b shows an enlarged view of the relevant part of the complex plane. A very close match between the dominant eigenvalues from the upstream and downstream data set is observed.
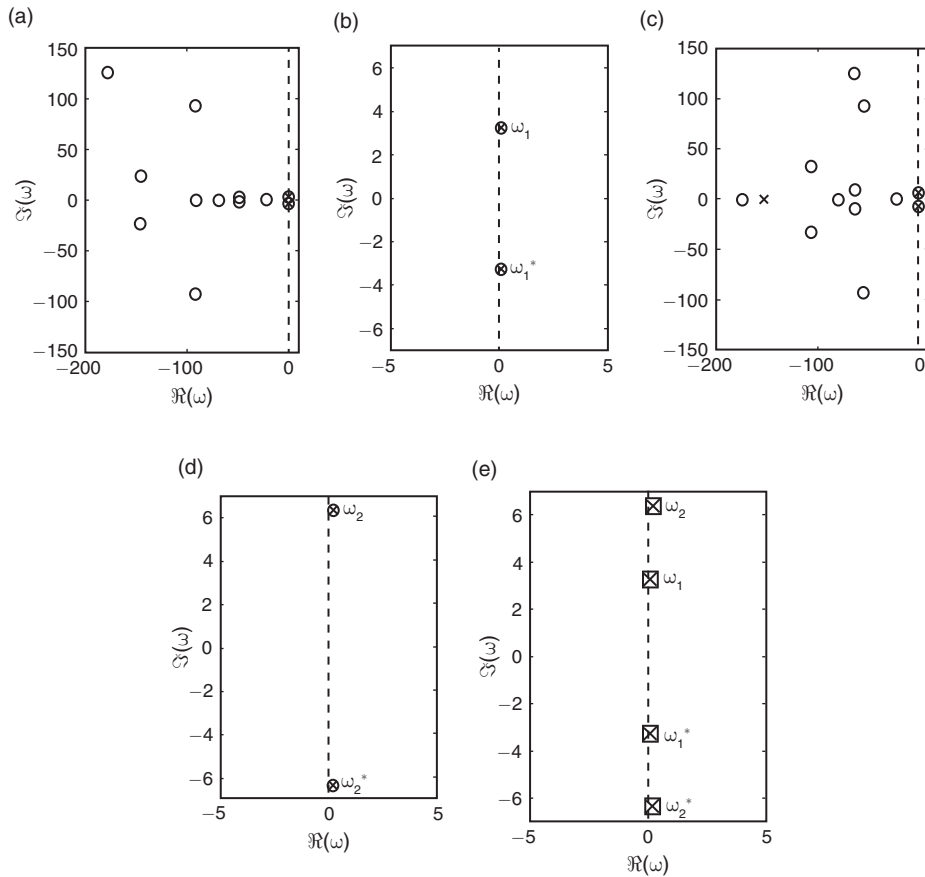
Figure 4: Eigenvalues obtained by applying DMD to data produced from (1). The decomposition is applied separately to data from the upstream and downstream side of the heater; the corresponding eigenvalues are displayed by symbols, × and ∘ respectively. Using (4), the initial condition consists of a first theoretical eigenmode in a and a second theoretical modes in b. A magnified view of the dominant eigenvalues is given in the right column. Finally, a comparison of the eigenvalues from theoretical investigations in □-symbols and from the DMD in ×-symbols is presented in (e) The governing parameters have been chosen as $n = 0.5, \tau = 0.2$ and $x_f = 0.125$.

After the upstream and downstream modes have been frequency-matched, continuity of the acoustic pressure across the heater is enforced and a composite eigenmode of the full system results. The second eigenmode of the system is calculated in an analogous manner from a data sequence, where the system (1) is initialized by the theoretical second eigenmode. Results of this calculation are displayed in figure 4c and d.

Figure 4*e* shows the eigenvalues of the first two modes, with the □-symbol representing the analytical eigenvalues and the ×-symbol illustrating the eigenvalues obtained from a data sequence via DMD. Good agreement between the two results is observed. The first two eigenmodes obtained by DMD are depicted in the right column of figure 3, where black dots are included to indicate the locations of the microphones. A discontinuity in the slope of the eigenmodes at the heater location is clearly visible, and an excellent match in the shape of the eigenmodes with the theoretical ones (see left column of figure 3) is observed. Furthermore, the amplitude of the inner product $|\langle p_1, p_2 \rangle|$ is in very good agreement between the extracted and theoretical eigenmodes.

Additional validation tests have been performed by extracting the dynamic modes, computing their rms-amplitude in the original data sequence, reconstructing the data sequence by a superposition of the most dominant dynamic mode and calculating the relative error between the original and reconstructed data sequence. The results are summarized in figure 5 for the first (left column) and second (right column) eigenmodes. The raw signal (figure 5*a, b*) is processed by the DMD which identifies two strong components for both the data set upstream (subfigure *c, d*) and downstream (subfigure *e, f*) of the heater. Higher dynamic modes are not represented in the original data sequence. As indicated in the second paragraph of this subsection, each eigenmode is extracted separately. The first two dominant dynamic modes represent a single eigenmode, along with its complex conjugate. Further, the initial conditions are chosen to have equal contributions in the eigenmode and its complex conjugate (see the caption of figure 5). Hence the amplitudes $||A_j||$ of the first two dynamic modes are same in figures 5(*c-f*). The
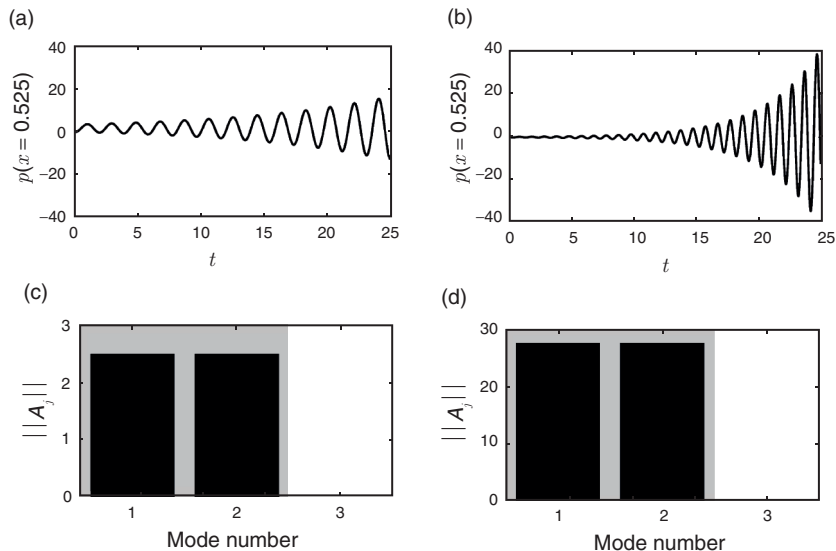
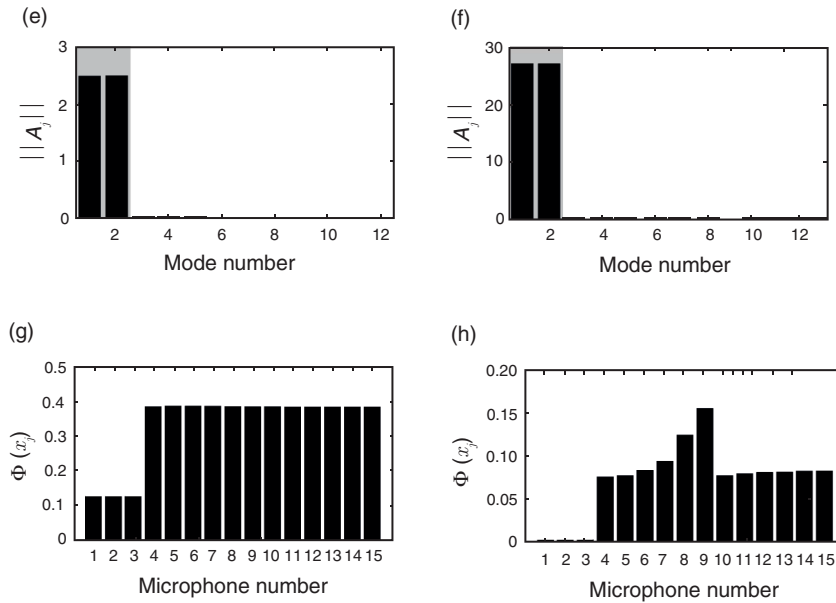

Figure 5 (Continued)

Figure 5:   Validation of the extraction of eigenmodes via the Dynamic Mode Decomposition. The subfigures on the left (right) hand side are associated with initial conditions along the first (second) mode. The initial condition is (*a*) $p(x, 0) = 0.6p_1(x) - 0.6p_1^*(x)$ and (*b*) $p(x, 0) = 0.3p_2(x) - 0.3p_2^*(x)$. The relative contribution (root-mean-square value) of the dynamic modes in the data sequence from the (*c*, *d*) upstream and (*e*, *f*) downstream side of the heater. The first two dynamic modes in each subfigure correspond to the actual eigenmodes. (*g*, *h*) The percentage difference $\Phi(x_j) = (||p(x_j, t) - p_r(x_j, t)||)/||p(x_j, t)|| \times 100$ between the input data and the reconstructed data sequence using the eigenmodes of the system at all microphone locations. The parameters are the same as in figure 4.

temporal data sequence reconstructed with only the most dominant dynamic modes (and their frequencies) is then compared to the original data sequence. In particular, the normalized difference between the original ($p(x_j, t)$) and reconstructed ($p_r(x_j, t)$) signal is calculated according to $\Phi(x_j) = (||p(x_j, t) - p_r(x_j, t)||)/||p(x_j, t)|| \times 100$. The results are plotted in figure 5(*g*, *h*). Less than a 0.4%-error is observed at all x_j-locations of the microphones for the first eigenmode; a maximal percentage error of 0.15% is observed for the second eigenmode.

A final test concerns the dependence of the non-orthogonality on the non-dimensionalized heater power n. The comparison between the theoretical results (solid line in figure 3) and the results obtained by DMD (symbols in figure 3) shows very good agreement over the entire range of heater powers, with a maximal deviation of 3.7% in the value of $(|\langle p_1, p_2 \rangle|)$ for $n = 0.55$.

Before applying DMD to the experimental data, it is important to assess the robustness of the above techniques with respect to noise in the measurements. In particular, the uncertainty in the final results as noise is added to the processed measurement data should be determined. Details of this procedure are given in Appendix B.

3.6. Transient growth experiment

The amount of transient growth depends on the exact shape of the initial condition. To observe transient growth, the initial condition given to the linear system must have non-zero projections onto at least two non-orthogonal eigenmodes [16]. In our case, this is achieved by exciting the system initially for a few cycles by a signal composed of two eigenfrequencies, obtained from the measured data by the DMD technique. The relative amplitude of the two frequencies can then be varied to construct various initial conditions; their transient amplification in time can then be monitored. It was observed by Matveev [7] and also from the current experiments, when the heat source is kept at $1/8^{th}$ of the axial location, then both the first and second modes are the least stable modes, while the third and higher modes are damped heavily. Hence, in the present case, we chose to use only the frequencies corresponding to the first two dominant modes.

4. RESULTS AND DISCUSSIONS

The techniques, tools and procedures introduced in the previous section will now be applied to our experimental setup of the Rijke tube. The experiments are performed at an ambient temperature of $296 \pm 1K$, with a relative humidity of $73 \pm 1\%$ such that the acoustic damping remains within required limits [38]. The exponential decay rate of the system is determined for a given frequency as follows.
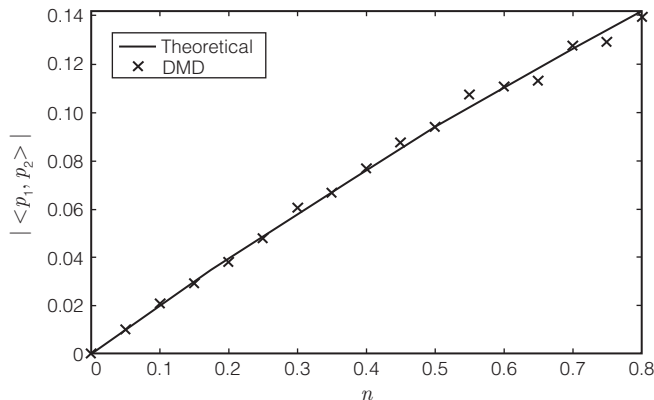

Figure 6:   Comparison of the non-orthogonality measure $|\langle p_1, p_2 \rangle|$ obtained from theoretical calculations (solid line) and from processing data by the DMD technique (symbols).
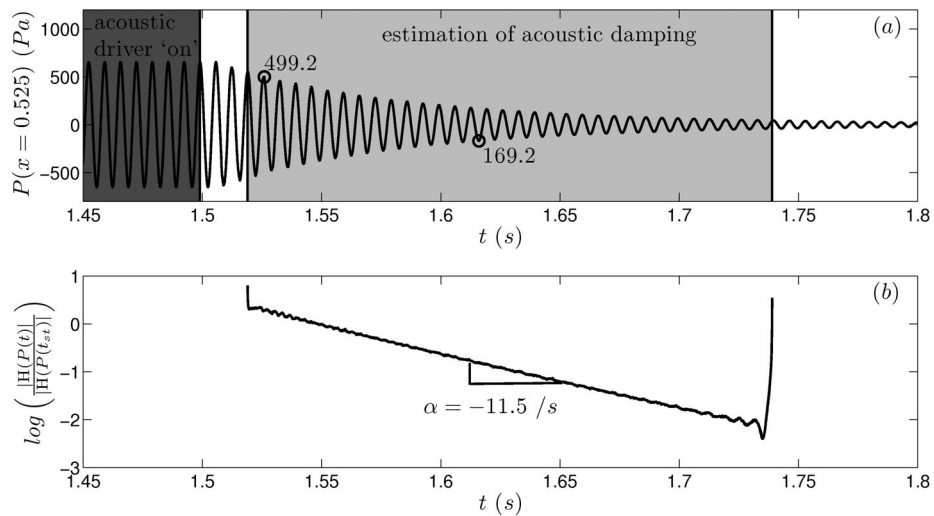
Figure 7:   Estimation of acoustic damping in the system. (*a*) Acoustic pressure measured at $x = 0.525$, which is used for damping measurement. Dark grey region indicates the period during which the acoustic driver is switched 'on' at a frequency of 156 Hz. Data used for the determination of acoustic damping is shown in light grey region. (*b*) Determination of the decay rate of the system by plotting the evolution of the logarithm of the instantaneous amplitude ratio $(log\,(|\mathrm{H}(P(t))|/|\mathrm{H}(P(t_{st}))|))$. The exponential decay rate (α) is obtained by the slope of the above curve.

In the cold flow, the system is excited for a brief period of time at the frequency of the first eigenmode, 156 Hz. After the acoustic driver is switched 'off', the system decays according to the decay rate corresponding to the first eigenfrequency. A typical acoustic pressure data at $x = 0.525$ is shown in figure 7 (*a*). Data used for the determination of acoustic damping is shown in light grey region. The instantaneous amplitude of the signal is obtained by the absolute value of the Hilbert transform of the signal [39]. The evolution of the logarithmic decay of the instantaneous amplitude, defined as $log\,(|\mathrm{H}(P(t))|/|\mathrm{H}(P(t_{st}))|)$ is plotted in figure 7 (*b*). t_{st} is the time at the start of the light grey region. The straight line part of the curve indicates the exponential decay of the instantaneous amplitude, whose slope gives the decay rate (α) of the system. In this case, the value of α is $-11.5/s$. This indicates that the signal drops to 1/e of its original value after approximately 13.5 cycles. Data points marked in figure 7 (*a*) are separated by 13.5 cycles and their ratio is 0.34, which is close to $1/e$.

Decay rates are measured at the start of the experiments. The experiments are further continued only when the decay rates are within $\pm 5\%$ of the previously stated value. This will ensure that the acoustic damping does not change appreciably from one experiment to another. The heater is located at $x_f = 0.125\ m$ for a Rijke tube of length $1\ m$. Following the series of steps outlined above, experiments are performed to initially obtain the bifurcation diagram, followed by the determination of the triggering amplitudes, after which the linear regime for the system is identified, the two most dominant eigenmodes are extracted, their non-orthogonality is established and the transient growth potential contained in these two modes is quantified.

4.1. Bifurcation diagram and triggering amplitudes

For the bifurcation diagram, the electrical power K supplied to the heater is chosen as the control parameter and the root-mean-square (rms) value of the acoustic pressure fluctuations $\left(P_{rms}\big|_{x=0.525}\right)$ at $x = 0.525$ is chosen as the variable that measures the state of the system. Figure 8 present the bifurcation diagrams for various mass flow rates $\dot{m}$.
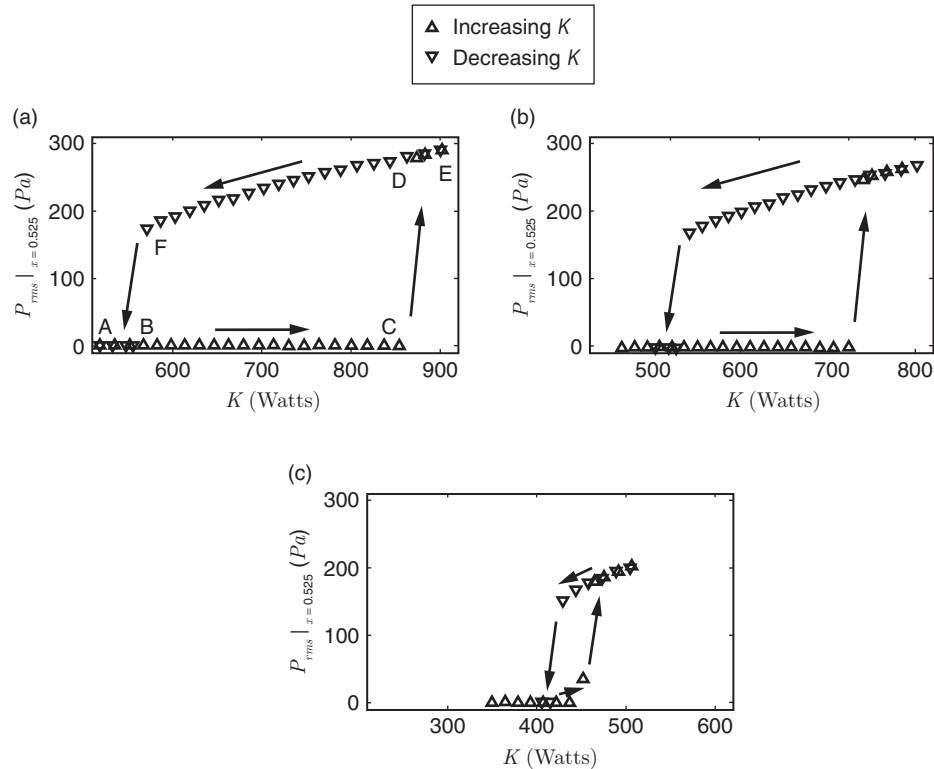

Figure 8: Bifurcation diagrams displaying the rms values of the acoustic pressure at $x = 0.15$ versus the power supplied to the heater. The mass flow rate is (*a*) $\dot{m} = 2.34\ g/s$, (*b*) $\dot{m} = 2.19\ g/s$, (*c*) $\dot{m} = 2.03\ g/s$.

Initially, the power supplied to the heater is low (point A in figure 8*a*) and the system is linearly and nonlinearly (globally) stable: the system reaches a steady state which is confirmed by monitoring the temperature at the inlet and further downstream ($x = 0.15$) of the heater. After about 30 minutes of preheating, the values of K and $P_{rms}|_{x=0.525}$ are noted. Next, the voltage supplied to the heater is increased by $0.05\,V$, which amounts to an increase in power of less than $20\,W$. This level of heating is maintained for 4 minutes to eliminate transients and allow the system to settle into a steady state [7]. In this manner, the power supplied to the heater is increased in a quasi-steady manner; raising the heater power more rapidly leads to nonlinear triggering of instabilities [7].

The time-asymptotic state of the system is recorded for increasing values of K and is termed the *forward path*. Analogously, the term *return path* is associated with decreasing values of K. The behavior of the system, as K is varied through a forward and backward path, is shown in figure 8(*a*). For low values of K (line AB), the system is globally stable. As the value of K is increased beyond point C (854 W), the system becomes linearly unstable and enters into a limit cycle (point D). Further increasing K yields progressively larger amplitudes of the limit cycle (line DE). On the return path, as the value of K is reduced from point E, the bifurcation curve retraces the forward path until point D after which it remains in the limit-cycle state up to point F (571 W). Beyond point F, the system falls back to the steady state. In summary, the return path (EDFBA) and forward path (ABCDE) are distinct, establishing the existence of common hysteresis behavior. Similar results have been reported [7].

From dynamical-systems point of view, the above transition scenario between globally stable and globally unstable behavior is referred to as *subcritical Hopf bifurcation* [40]. Within the hysteresis zone (BCDF), the system is linearly stable. However, an initial threshold amplitude exists (termed *triggering amplitude*) above which the system becomes unstable and approaches limit-cycle behavior. This regime is also termed as bistable region, as two stable solutions i.e., steady state and limit cycle are possible.

Experiments at different mass flow rates $\dot{m}$ reveal that the hysteresis zone becomes smaller (figure 8 *b,c*) as the flow rate decreases (see also Matveev [7]). For our study of the non-normal nature of the system, we will concentrate on the case with the largest hysteresis zone and choose $\dot{m} = 2.34\,g/s$. The steady state flow velocity (u_u) upstream of the heater and the Reynolds number (Re) based on the diameter of the wire in the mesh are 0.24 m/s and 4.2 respectively.

The triggering amplitudes have been obtained by first allowing the system to attain a steady state within the hysteresis region after which an initial acoustic pulse train is fed to the system using the acoustic driver units. The pulse train consists of 14 cycles of a sinusoidal wave at a frequency equal to the first eigenfrequency of the system. The amplitude of the input wave is increased until the system changes from a linearly stable state to a nonlinearly unstable state. For excitations with the frequency of the second eigenmode, higher triggering amplitude is required to render the system nonlinearly unstable; hence, the triggering amplitudes have been estimated by exciting only the first eigenmode. Figure 9*a* presents the evolution of the system for a case where the initial excitation is sufficient to trigger the system into a nonlinearly unstable state. The inset
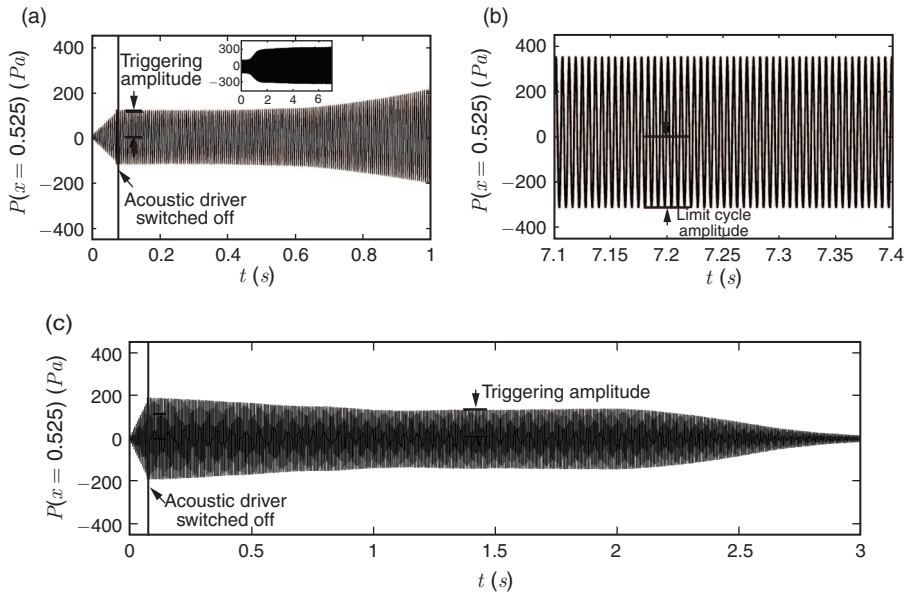
Figure 9:   Determination of triggering and the corresponding limit cycle amplitudes. (*a* & *b*). Evolution of the system that is just triggered and (*c*) just decayed. $K = 782$ W, $\dot{m} = 2.34$ g/s.

confirms that the excited system ultimately reaches a limit cycle. The initial $P_{rms}|_{x = 0.525}$ (after the acoustic drivers are switched off) is noted as the triggering amplitude. The associated resulting limit cycle is shown in figure 9(*b*) and the value of $P_{rms}|_{x = 0.525}$ is recorded as well. On the other hand, figure 9(*c*) represents the evolution of the system that just fail to trigger and eventually decay to a stable fixed point.

The above procedure for finding the triggering and limit cycle amplitudes has been repeated for various values of K and the obtained results are shown in figure 10. The bifurcation diagram is labeled, as before, by the characteristic points ABCDEF. In addition, the triggering and corresponding limit cycle amplitudes are designated by GH and IJ, respectively. For each value of K the experiment has been repeated four times to control and quantify measurement inaccuracies. Consequently, the limit cycle amplitudes in the bifurcation diagram have been found to vary by less than ±0.5%. Results near the Hopf (C) and fold (F) points of the diagram could be determined within a band of 40 W and 26 W, which amounts to less than 4.5% of the power levels at the respective points. Furthermore, the spread in the triggering amplitudes and corresponding limit cycle amplitudes is less than ±6% of the respective mean values.

Triggering amplitudes beyond H have not been attempted since the spread prescribed above could not be maintained in this parameter regime due to an increasing sensitivity near the Hopf point [40]. Also, the acoustic drivers failed to trigger the system into a nonlinearly unstable state below point G; thus no results are reported below point G. The amplitude of the limit cycle (IJ) obtained by triggering the system
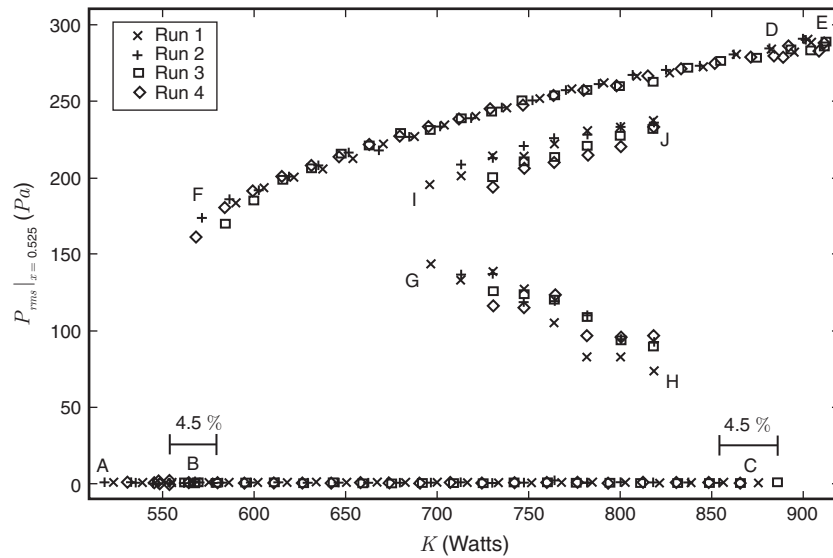
Figure 10: Bifurcation diagram showing hysteresis behavior along with the triggering (GH) and limit cycle (IJ) amplitudes. The experiments have been repeated four times to ensure repeatability of the results. A mass flow rate of $\dot{m} = 2.34 \ g/s$ has been chosen.

is smaller than that obtained from the bifurcation diagram (FD). This discrepancy can be attributed to the difference in the mean temperature in the duct during the phase of increasing and decreasing (path ABCDE and EDFBA in figure 8) heater power as shown in figure 11. The higher mean temperature is due to non-zero mean heat transfer effects occuring during intense thermoacoustic oscillations; this phenomenon has also been observed by Matveev [7].

4.2. Regime of linearity

The bifurcation diagram is further augmented by determining the parameter regime where the system dynamics can be well approximated by a linear process. This is accomplished by measuring the response of the system to continuous excitation by the acoustic driver units and comparing it to expected results based on theoretical scalings. The details of the procedure are presented in Appendix A. As a result, we obtain critical pressure amplitudes below which the system performs nearly linearly and above which nonlinear effects become no longer negligible. These critical amplitude levels (as the power supplied to the heater is varied) define the limit of linearity. It is shown in figure 12 along with the triggering amplitude and labeled by LN. Curves GH and IJ represent the mean value of the triggering and the corresponding limit cycle amplitudes averaged over different experiments (shown previously in figure 10). It is evident from figure 12 that the linear regime, indicated
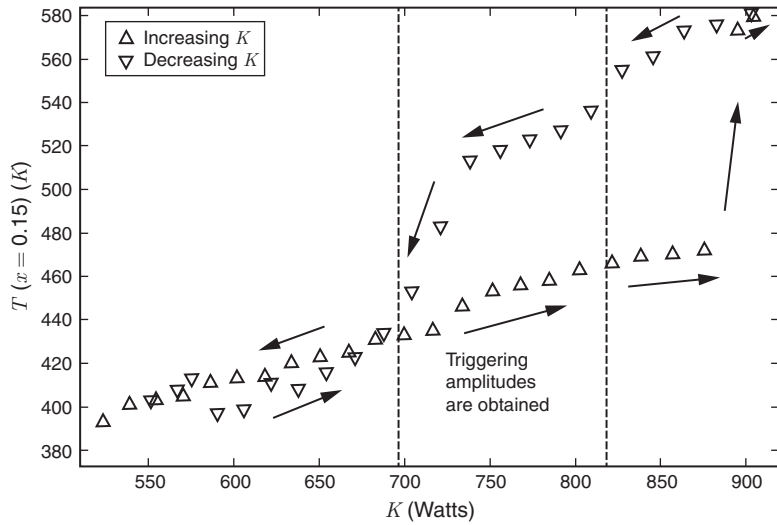
Figure 11:   Steady state temperature recorded downstream of the heater during experimental run 1. The steady-state temperature during increasing and decreasing values of K are shown. Vertical dashed lines indicate the power level associated with the region IJ shown in figure 10.
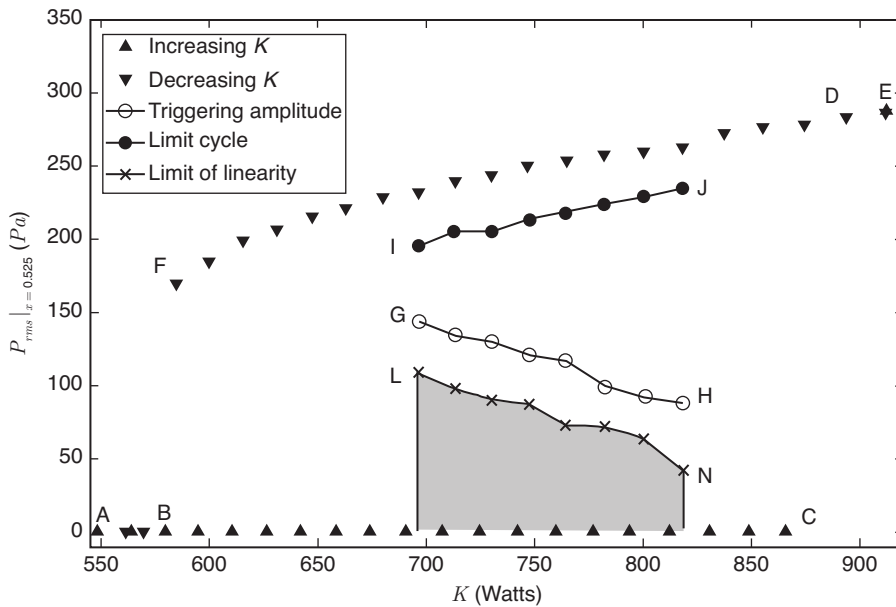

Figure 12:   Bifurcation diagram showing averaged triggering amplitudes (GH) and averaged limit cycle amplitudes (IJ). The limit of the linearity (LN) defines the linear regime (in gray); all experiments investigating the non-normal nature of the thermoacoustic system are performed in this regime.

in gray, covers a rather large area in the bifurcation diagram — measurements can thus be obtained with high signal to noise ratio.

4.3. Non-orthogonality of the eigenmodes

Acoustic pressure data recorded by the microphones are used for the DMD analysis where a total of 742 snapshots (with $0.125 \ ms$ as the time interval between them) have been processed. The amplitudes of the recorded acoustic pressure is below the linearity limit defined in Appendix A. As described in section 3.3, a measure of non-orthogonality of the eigenmodes is given by the expression $|\langle p_1, p_2 \rangle|$. The effect of measurement noise on the value of $|\langle p_1, p_2 \rangle|$ is discussed in Appendix B.

The eigenmodes and corresponding values of $|\langle p_1, p_2 \rangle|$ obtained from experimental data are displayed in figure 13(*a-c*). The first and second eigenmodes are obtained through individual self-excited experiments. The reason is as follows. As indicated in the second paragraph of section 3.5, DMD technique is applied separately in the sections upstream and downstream of the heater. In the upstream side, there are three microphone ports (table 1) and hence only three dynamic modes are obtained. Among
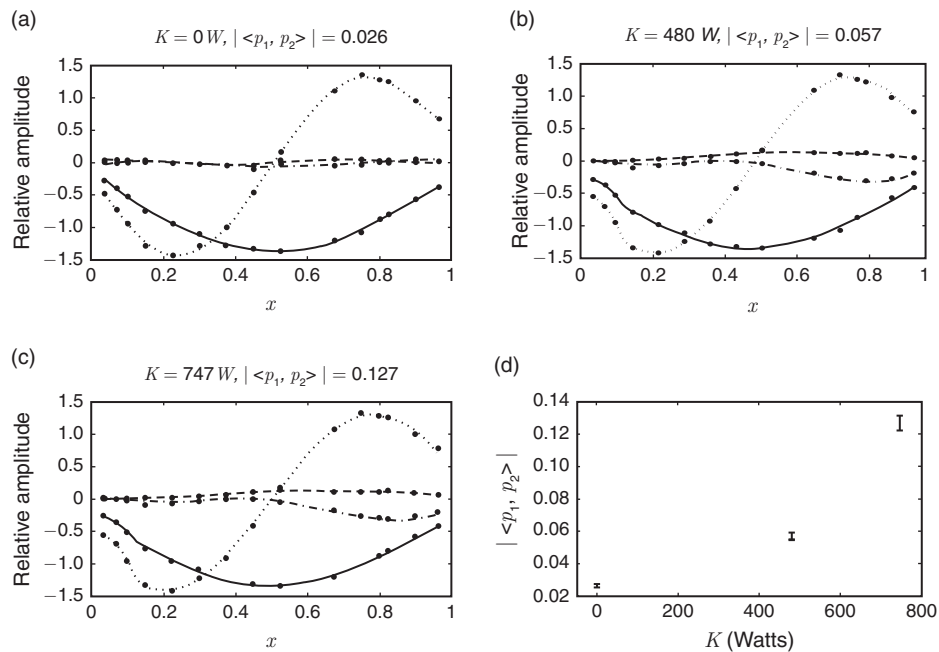

Figure 13: (*a-c*) First two dominant eigenmodes obtained by applying DMD to the experimental acoustic pressure data. The respective values of the heater power K and the absolute value of the inner product $\langle p_1, p_2 \rangle$ are indicated in the title of each subfigure. Legends and symbols are identical to the one in figure 3. (*d*) Dependence of $|\langle p_1, p_2 \rangle|$ on the power supplied to the heater K, together with the associated error bars.

this, the two dominant ones represent a single eigenmode, along with its complex conjugate. Hence two separate experiments have to be conducted to determine the first two eigenmodes. In order to excite the system in a given eigenmode (in experiments), the following technique is followed. The system is initially forced for a brief period of time at a frequency close to the frequency of a particular eigenmode. After the excitation is turned off, the system evolves as a self excited one. In this manner, the required eigenmode (nearly exclusively) is excited.

As the power supplied to the heater is increased, the discontinuity in the slope of the eigenmodes at the heater location becomes more noticeable. In addition, the non-orthogonality measure $|\langle p_1, p_2 \rangle|$ increases steadily with increasing values of K. The uncertainty in the value of $|\langle p_1, p_2 \rangle|$ is at most $\pm 2.5\%$ for the noise levels encountered in our experiments (see Appendix B for details). The variation of $|\langle p_1, p_2 \rangle|$ with heater power K is shown in figure 13d along with the associated error bars and confirms a significant rise in non-orthogonality as the power supplied to the heater is increased. It is to be noted that the eigenmodes obtained from the theoretical system assumes no steady state temperature gradient in the system. While in the actual system (experiments), there is a temperature gradient due to the presence of the heater. The shape of the eigenmodes is influenced by the temperature profile [41]. Due to this, we believe that the difference in the shape of the eigenmodes between the theoretical (figure 3) and experimental (figure 13) system.

As in section 3.5, we verify that the extracted dynamic modes indeed represent the eigenmodes of the system. Figures 14(a, b) show typical acoustic pressure signals measured at the upstream and downstream side of the heater which are used for the
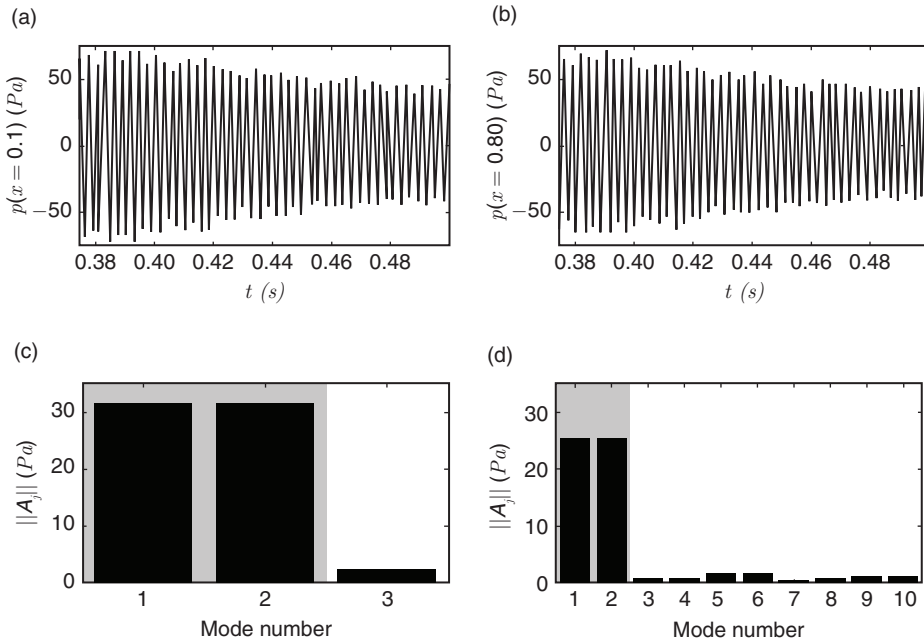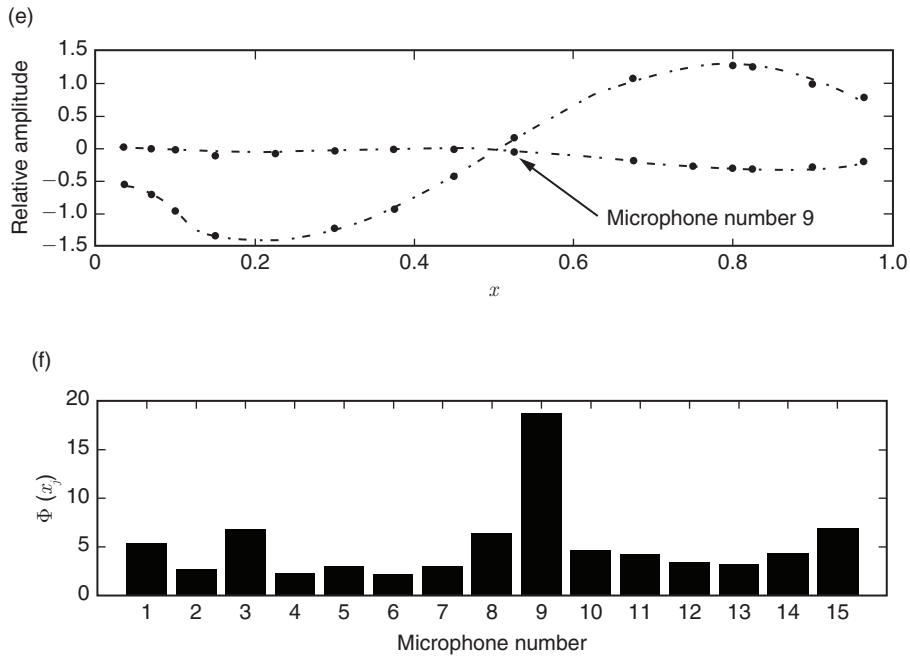

Figure 14 (Continued)

(e)

(f)

Figure 14:   Experimental acoustic pressure data at (*a*) location $x = 0.1$ and (*b*) location $x = 0.8$ which is used in the DMD-analysis. The initial condition is closely aligned in the direction of the second eigenmode of the system. The relative contributions (root-mean-square value) of the dynamic modes to the full data sequence for the (*c*) upstream and (*d*) downstream side of the heater. The first two dynamic modes, along with their complex conjugates, represent the second eigenmode of the system. (*e*) The spatial structure of the first dynamic mode with '········' signifying the real part and '· − · − ·' the imaginary part. (*f*) The relative error (in percent) at all locations of the microphones, $\Phi(x_j) = (||p(x_j, t) - p_r(x_j, t)||)/||p(x_j, t)|| \times 100$, between the input data p and a reconstructed data sequence p_r using the first two dynamic modes.

extraction of the second eigenmode of the system. The system is initially forced for a brief period of time at a frequency close to the frequency of the second eigenmode. After the excitation is turned off, the system evolves as a self excited one. In this manner, the second eigenmode (nearly exclusively) is excited. The contribution of the most relevant dynamic modes to the data sequence is shown in figure 14 (*c*, *d*); only the first two dynamic modes figure significantly in each data sequence. The spatial structure (with real and imaginary components) is depicted in figure 14 (*e*). Lastly, acoustic pressure data are reconstructed based on only the second eigenmode and are compared to the original data sequence. The relative error between the two time series, evaluated at each microphone location, is displayed in figure 14 (*f*), where an error of less than 7% is observed at all but one microphone locations. The 9th microphone is

located close to the acoustic pressure node of the second eigenmode and thus experiences a substantially lower signal-to-noise ratio and a relative error of 19%. A deviation of less than 7% suggests that the dynamics is well represented by the extracted second eigenmode of the system.

4.4. Evidence of transient growth

After the non-orthogonality of the two dominant eigenmodes has been established, the amount of transient amplification of acoustic energy will be determined. The total acoustic energy (dimensional) is defined as $\tilde{E}(t) = \dfrac{S_c}{2} \displaystyle\int_0^L \left(\overline{\rho} u^2 + p^2 / \left(\gamma \overline{p} \right) \right) dx$ and has previously been used in theoretical studies on the same Rijke tube system [10]. In the above expression, S_c denotes the cross-sectional area of the tube and the overbar $\overline{}$ represents steady-state quantities. The acoustic pressure p is measured at the 15 locations (see figure 2 and table 1), and the acoustic velocity u is obtained by a two-microphone technique [42]. The largest spacing between any two microphones in the present experiment is 75 mm and the cross-sectional dimension is 92 mm which allows us to measure acoustic velocity fluctuations in the frequency range 100 Hz to 1.76 kHz [43]. For our interest in the first ($\approx 175\ Hz$) and second ($\approx 350\ Hz$) eigenmodes of the system, the inter-microphone spacing is suitable for our experimental investigation.

Three kinds of initial perturbations are considered in our analysis. The first two initial conditions correspond to a harmonic excitation with a pure frequency of the first two respective eigenmodes, while the waveform of the third kind of initial perturbation consists of a linear combination of the first two eigenfrequencies of the system.

For each setting of the heater ('on' and 'off'), the evolution of the system excited by the three initial conditions is analyzed. When the heater is switched off, the non-dimensional acoustic energy ($E = \tilde{E}/[S_c \rho_u u_u^2/2]$ with subscript $_u$ representing the steady-state quantities on the upstream side of the heater) decays continuously in time after the excitation from the acoustic driver ceases, shown by the vertical black line (see figure 15a). The grey area indicates the region, where the forcing from the acoustic driver is present. The normalized amplification of acoustic energy $E(t)/E(0)$ (where the origin of the time-axis is shifted to the instant when the excitation from the acoustic speaker stops) is plotted in figure 15(b). No significant transient growth can be observed in cold flow for any of the initial conditions, indicating that the dynamics of the pure acoustic field is normal.

For the case with a heater power of 747 W, no significant transient growth can be detected when the system is excited by the first two initial conditions (as shown in figure 15c) since almost a pure eigenmode is excited. On the other hand, when the initial condition contains non-zero components in the two eigenmodes, transient growth (indicated by the solid curve in figure 15c) is clearly visible. The relative energy amplificiation can be seen in figure 15d; for the specific initial condition, it amounts to 1.8 times the initial energy. This growth in energy is comparable to numerical studies [10, 44, 13].

To rule out nonlinear effects and be able to attribute the measured energy amplification to the non-normal nature of the thermoacoustic system, we have to ensure that the measured pressure amplitudes remain within the linear regime for all times.
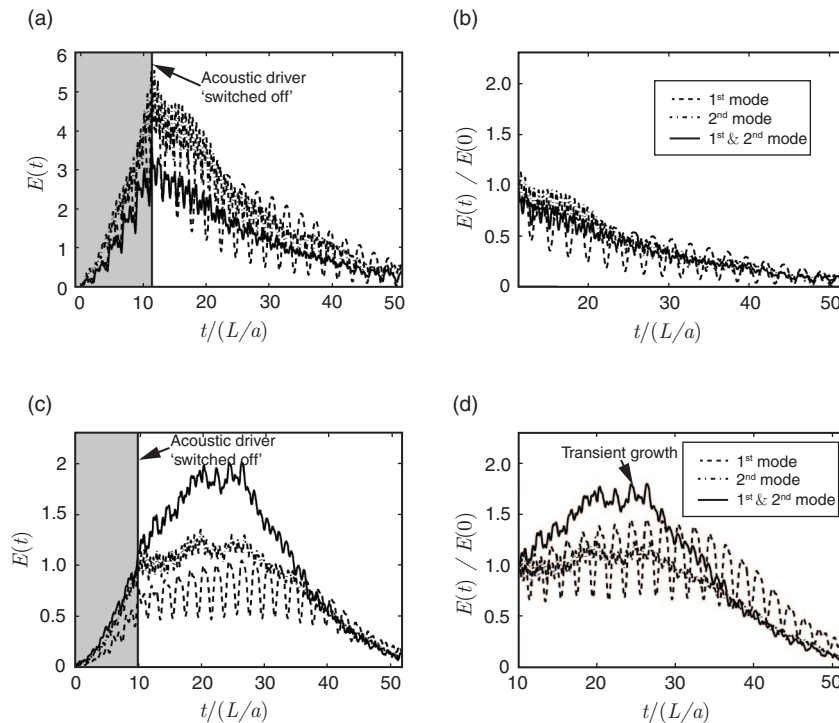
Figure 15: Evolution of non-dimensional acoustic energy defined as
$$E(t) = \int_0^L \left(\rho u^2 + p^2 / (\gamma p_u) \right) dx \,/ \left(\rho_u u_u^2 \right).$$ For (a), the heater is switched off; for (c), the heater is switched on ($K = 747\ W$). Evolution of the normalized amplification of acoustic energy $E(t)/E(0)$ with heater switched off (b) and switched on (d). The time interval during which the acoustic driver is active is indicated in gray.

Figure 16(a) displays the acoustic pressure signal which corresponds to the transient growth in figure 15c for the composite initial condition (third kind). The two horizontal dash-dotted lines indicate the limit of linearity. To further confirm the linear nature of the system output, a simple scaling experiment has been conducted: the initial perturbation amplitude is scaled by a factor 0.75 and 0.5 and the associated evolution of the pressure is recorded (see figure 16b and c, respectively). These two pressure measurements are then rescaled and compared to the original pressure measurements. The close match (of less than 3%), displayed in figure 16d, confirms that the transient effects shown above are void of nonlinear contributions and can thus be ascribed to the non-normal character of our system.

4.5. Optimal initial condition
Motivated by the results of the previous section, it remains to determine the maximum transient growth potential contained in the two dominant eigenmodes by varying their
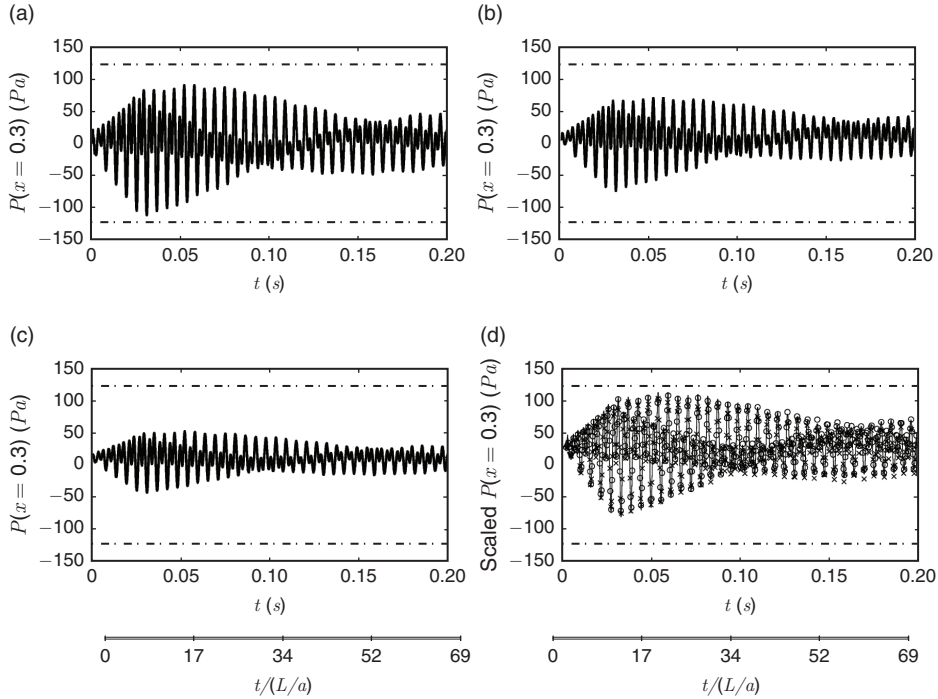
Figure 16:   Evolution of the acoustic pressure at $x = 0.3$ in the linear regime. The two horizontal dash-dotted lines in all subfigures represent the amplitudes delimiting the linear regime. The amplitude of the initial perturbation is scaled and the subsequent evolution of the system is recorded: (*a*) for $0.1\sin(2\pi f_1 t) + 0.1\sin(2\pi f_2 t)$, (*b*) for $0.075\sin(2\pi f_1 t) + 0.075\sin(2\pi f_2 t)$, (*c*) for $0.05\sin(2\pi f_1 t) + 0.05\sin(2\pi f_2 t)$. In (*d*) the acoustic pressure signals from subfigures (*a*)-(*c*) are rescaled and superimposed. Circle and cross symbols are associated with data from subfigures (*b*) and (*c*), respectively. The duration of the system's evolution is taken as $0.2s$, which corresponds to a non-dimensional time span $t/(L/a)$ of 69. f_1 and f_2 are the frequencies of the first and second eigenmodes of the system. The supplied heater power is $K = 747 \ W$.

relative amplitude and phase angle in the initial condition. To this end, a more general input perturbations is forced upon the system; we take it of the form $A_1\sin(2\pi f_1 t) + A_2\sin(2\pi f_2 t + \theta)$. As before, f_1 and f_2 stand for the frequencies of the first and second eigenmodes of the system; the amplitudes of the respective eigenmodes are denoted by A_1 and A_2. The phase angle between the two sine waves is given by the variable θ. The maximum of the energy amplification $E(t)/E(0)$ over time is represented by $E_{\mathrm{max}} = \max_t E(t)/E(0)$.

Figure 17*a* displays the variation of E_{max} with the amplitude ratio A_2/A_1 for a fixed phase angle of $\theta = 0°$. The symbols ($\times$) represents the experimental data; the continuous
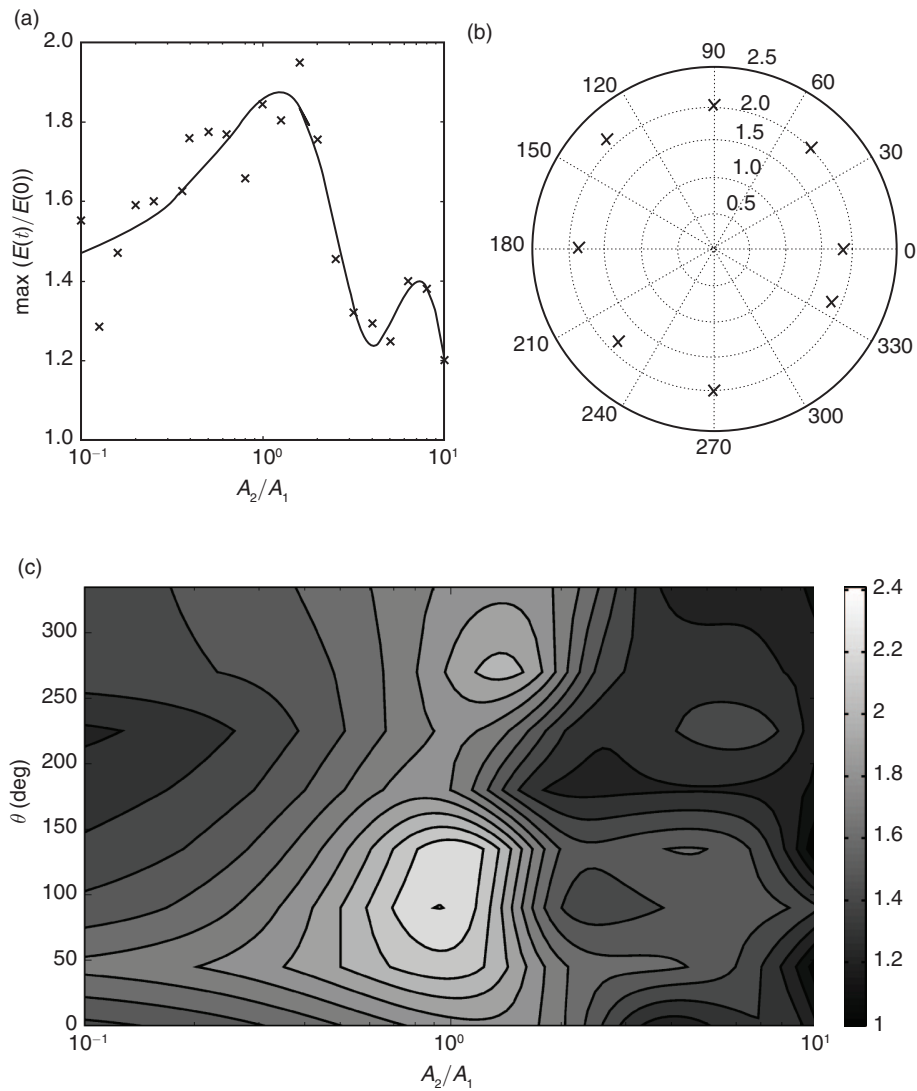
Figure 17:   Variation of the maximum energy amplification E_{max} with (*a*) amplitude ratio A_2/A_1 for fixed phase angle $\theta = 0°$ and (*b*) with phase angle θ for fixed amplitude ratio $A_2/A_1 = 1$. The symbols ($\times$) indicate the experimental data point; the continuous line represents a Gaussian fit. (*c*) Maximum transient growth over initial conditions of the form $A_1\sin(2\pi f_1 t) + A_2\sin(2\pi f_2 t + \theta)$ The optimal initial condition for maximum transient growth is identified for the parameter combination $A_2/A_1 = 0.93$ and $\theta = 90°$. The corresponding maximum transient growth is 2.3. The remaining parameters are $f_1 = 173\,Hz$, $f_2 = 346\ Hz$, $\dot{m} = 2.34\ g/s$ and $k = 747\ W$.

line shows a Gaussian fit of the data. Maximum amplification occurs at $A_2/A_1 = 0.85$, i.e., at an amplitude ratio where the initial condition has comparable contributions from either eigenmode. The value of E_{max} decreases markedly away from the optimal value. This observation also reinforces the fact that the amount of transient growth has to diminish as the initial conditions progressively contains only contributions from one of the two eigenmodes. To complement, the variation of E_{max} with phase angle θ for a fixed amplitude ratio of $A_2/A_1 = 1$ is shown in figure 17(*b*) in form of a polar plot. For this parameter setting, the value of E_{max} is nearly independent of θ. The complete parameter dependence (simultaneously varying A_2/A_1 and θ) is depicted as a contour map in figure 17(*c*). Two local maxima have been found; the global maximum of transient growth appears for an initial condition with an amplitude ratio of $A_2/A_1 = 0.93$ and a phase angle of $\theta = 90°$. The associated maximum transient growth is $E_{max} = 2.3$.

4.6. Triggering energy

In a final step, we explore the triggering energies for initial conditions composed of the two eigenmodes with varying amplitude ratio A_2/A_1 and phase angle θ by increasing the amplitude of the initial amplitude until a limit cycle is reached. Figure 18(*a*) (see also
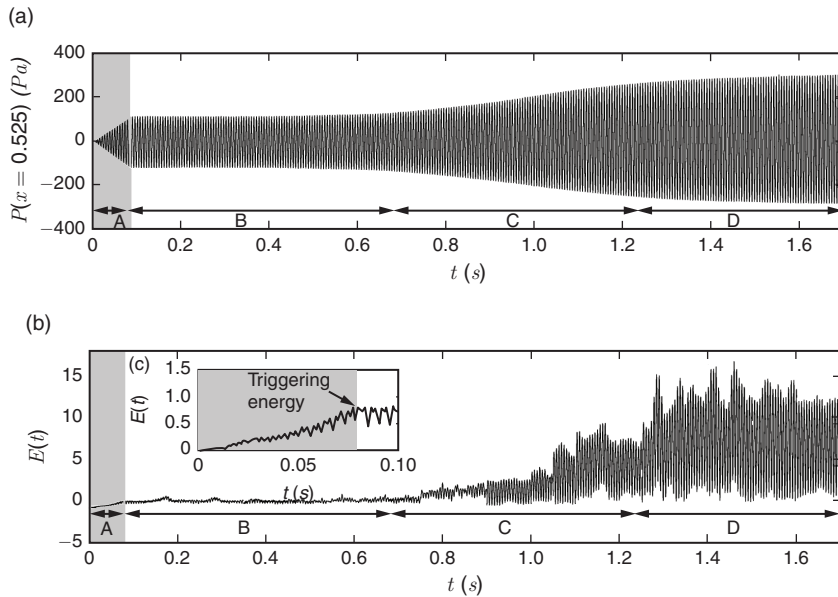

Figure 18: Evolution of (*a*) acoustic pressure $P(x = 0.525)$ and (*b*) acoustic energy $E(t)$ for the triggering of an instability. The inset (*c*) shows the initial evolution of $E(t)$ Zones A, B, C and D represent the time intervals where the system is excited by the acoustic driver (A), near the triggering amplitude (B), in the nonlinearly unstable state (C) and in the final limit cycle (D). The gray area represents the region when the acoustic driver is switched on. The governing parameters are $A_2/A_1 = \theta = 0°$, $K = 782$ W and $\dot{m} = 2.34$ g/s.

figure 9*a*) shows a typical time history of acoustic pressure for such an experiment; in the companion figure 18(*b*), the acoustic energy $E(t)$ is displayed. The various phases toward a final limit cycle are also indicated qualitatively in both subfigures. For slightly lower amplitude, but otherwise constant parameters, the oscillations decay asymptotically to zero. The experiment can thus be assumed near the triggering threshold. As before, the grey area indicates the time span during which the acoustic driver is active.

The value of $E(t)$ increases steadily in region A as the system is excited during this period. In zone B, the energy $E(t)$ remains nearly constant. In the subsequent zone C, the energy increases further as the trajectory is repelled from the unstable limit cycle [40]. Eventually, the system reaches a stable limit cycle, marked as zone D, where $E(t)$ remains almost constant at a higher value compared to that of the other zones. In the above case, the initial condition has been selected with $A_2/A_1 = 0$ and $\theta = 0°$. The inset in figure 18*b* shows more details of the evolution of $E(t)$ in zone A. Since $E(t)$ is strongly fluctuating, the triggering energy E_{trig} is determined by time-averaging $E(t)$ over a period $1/f_1$ immediately before the instant when the acoustic driver is switched off.

The variation of E_{trig} with A_2/A_1 for fixed $\theta = 0°$ is shown in figure 19*a*. Since the determination of E_{trig} is rather sensitive to the ambient noise in the system, experiments
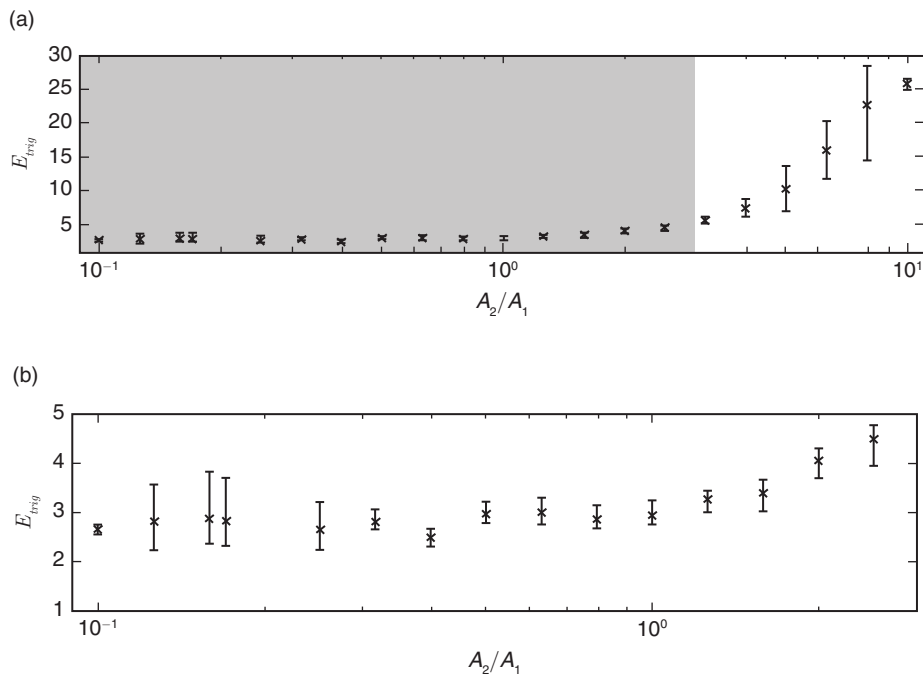
(a)

(b)

Figure 19: (*a*) Acoustic energy E_{trig} required for triggering an instability as a function of amplitude ratio A_2/A_1 (*b*) Magnified version of (*a*) for a value of A_2/A_1 between 0.1 and 3.0. This parameter interval is shown in gray in (*a*). The remaining parameters are $\theta = 0°$, $K = 747\ W$ and $\dot{m} = 2.34\ g/s$.

are repeated three times (cf. section 4.1) and the mean value, along with the associated deviation, is reported. For low values of A_2/A_1, i.e., initial conditions with predominant contributions from the first eigenmode, less energy is required to trigger the system into a limit cycle. The value of E_{trig} increases rapidly beyond an amplitude ratio of $A_2/A_1 = 3$ and the system requires higher triggering energies as the contribution from the second eigenmode becomes more prevalent. A close-up view of the region before the sharp rise in E_{trig} is presented separately in figure 19(b). It can be established that E_{trig} is nearly constant until approximately $A_2/A_1 = 1.6$; the lowest triggering energy E_{trig} is recorded for $A_2/A_1 = 0.4$ with a spread of $\pm 6\%$ around its mean value.

From figure 17(a), the optimal initial condition (with $\theta = 0°$) for maximum transient growth occurs for $A_2/A_1 = 1.6$ and while the triggering energy E_{trig} in figure 19(a) shows no particular preference for this value of the amplitude ratio A_2/A_1. It appears that the role of transient growth around the stable fixed point, undoubtedly present in the thermoacoustic system, plays a minor or insignificant role in the subcritical transition regime. The following may be possible reasons for this observation.

First, the true difference in value of E_{trig} as a function of A_2/A_1 (which is responsible for the selection of a preferred amplitude ratio) might be noticeably smaller than the error bar obtained in the present investigation. Secondly, and more importantly, our optimal initial condition has been restricted to linear combinations of the first two eigenmodes of the system. For the particular case examined by Juniper [13], the optimal initial condition had distinct contributions from the third and fourth eigenmodes, but little from the second. It is possible, however, that different parameters (such as heater position) could change this. This has yet to be tested. For our experimental setting, the third eigenmode is highly stable compared to the first two eigenmodes and extracting this mode, simultaneously with the first two eigenmodes, in the linear regime will encounter very low signal-to-noise ratios and thus prohibit any definite conclusions regarding its role in subcritical transition. In view of these difficulties, the role of transient growth in the subcritical transition regime remains open — from an experimental point of view. Nonetheless, the non-normality of our thermoacoustic system, the notable increase in the non-orthogonality of the eigenmodes with heater power and the evidence of associated transient growth have been clearly identified in our experiments.

5. SUMMARY AND CONCLUSIONS

Experiments have been performed to identify and probe the non-normal nature of thermoacoustic interactions in an electrically heated, horizontal Rijke tube. As the power supplied to the heater is increased, the transition from linearly stable to unstable behavior occurs via a subcritical Hopf bifurcation. This transition is aided by transient growth of acoustic energy in the tube, a phenomenon that has been established and investigated theoretically. Since transient growth is a linear phenomenon, experiments have to be performed in a parameter regime where the system behaves nearly linearly. In addition, only the linearly stable regime can be explored to ensure linearity for all times.

Measurements of the acoustic pressure have been processed via the Dynamic Mode Decomposition (DMD), a data-based technique that extracts dominant eigenmodes from measurement sequences of a linear process. It has been demonstrated that the

non-orthogonality of the obtained eigenmodes increases as more power is supplied to the system by the heater. This behavior confirms the non-normal nature of thermoacoustic interactions in the Rijke tube. The amount of resulting transient growth has been measured in terms of the acoustic energy composed of the measured acoustic pressure and the acoustic velocity, calculated via a two-microphone technique. With the heater switched on, no significant transient growth is observed when the system is excited with an initial condition that has projection along only one of the two dominant eigendirections; transient growth, causing a two-fold increase in acoustic energy, has been observed, however, when the initial condition contains contributions from both eigenmodes. For cold flow (with the heater switched off), no significant transient growth has been found for any initial perturbations, indicating that the classical linear acoustic system is normal.

A parameter study, varying amplitude ratio and phase angle of the two initial eigendirections, revealed a maximum transient amplification of acoustic energy of 2.3 which has been obtained for an amplitude ratio $A_2/A_1 = 0.93$ and a phase angle of $90°$. An analogous parameter study of the threshold acoustic energy E_{trig} for triggering limit-cycle behavior (for $\theta = 0°$) showed a low and constant value for $0.1 < A_2/A_1 < 1.6$, after which it rises steadily. A link between parameter combination, for which maximum transient growth can be observed, and parameter combinations, for which the triggering energy is particularly low, could not be established. The restriction to only two dominant eigendirections (which could be extracted from measurements with sufficient confidence in their accuracy) is expected as the reason for this discordance and is corroborated by previous theoretical studies. Nonetheless, the non-normal nature of the thermoacoustic system and the associated transient growth in acoustic energy has been clearly identified by experimental means.

6. ACKNOWLEDGMENTS

A. Experimental determination of the linear regime

In order to identify the linear regime for our experimental setup, it is important to first characterize the acoustic drivers regarding their linearity. The equations governing the classical acoustic field in a duct are linear [45]. The Rijke tube system is continuously excited at a given frequency using acoustic drivers, with the heater and blower switched off, and the response of the system is recorded by the microphones. The voltage supplied to the acoustic driver is also noted and varied. This way, a response curve for the acoustic driver unit is obtained; it is shown, for three forcing frequencies, in figure 20. On the horizontal axis, the rms-value of the voltage supplied to the acoustic driver units is shown; on the vertical axis, the rms-value of the acoustic pressure fluctuations ($P_{rms}|_{x=0.525}$) is displayed. The symbols indicate the experimental data, the
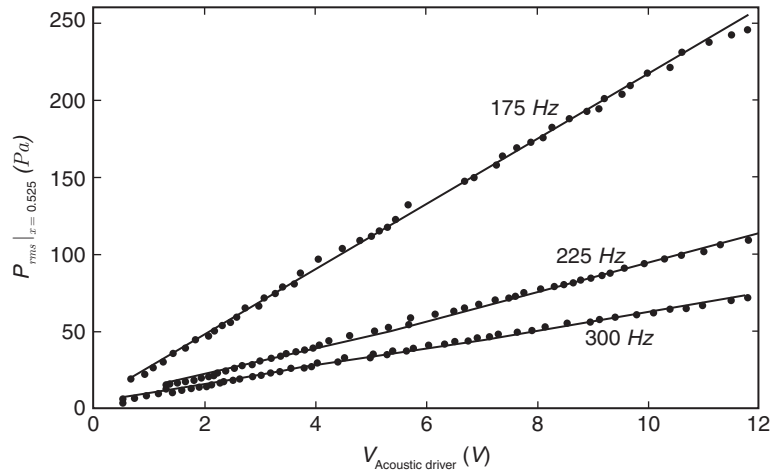
Figure 20:   Characteristics of the acoustic driver unit, obtained for three different frequencies. The rms-value of the voltage supplied to the acoustic driver unit is indicated on horizontal axis. The symbols represent the experimental data, while the continuous line presents a linear fit of the data.

lines present a linear fit. From the response curve, one can conclude that the linear fit represents the experimental data with less than a $\pm0.25\%$ spread. Hence, for the voltage range covered in figure 20, the relation between the voltage supplied to acoustic driver and the generated acoustic pressure can be assumed linear.

The heater and blower are now turned on. Due to reasons explained in section 4.1, the linear regime is identified only within the zone GH. Figure 21 presents the response of the system to continuous excitation with the acoustic driver, where the output is given by the rms-value of acoustic pressure fluctuations. As before, the symbols indicate the experimental data. It can be noted that the symbols do not form a straight line; rather, a sublinear relation for larger amplitudes of the voltage can be detected. The dashed line represents a power-law fit to the experimental data (with a spread of $\pm0.15\%$). A linear fit, shown as a continuous line, is performed on part of the experimental data for low amplitudes of $V_{\text{Acoustic driver}}$ (in our case less than 3 V). Additionally, the triggering amplitude is marked as a dash-dotted horizontal line. The limit of linearity is then determined as the point when the deviation of the experimental data from the linear fit exceeds 5% of the corresponding triggering amplitude. The amplitude, at which the nonlinear nature of the system comes into play, is given by the triggering amplitude; hence, it is taken as the reference quantity. The linear regime defined above is indicated in grey in figure 21.

B. Application of DMD in the presence of noise

The application of the DMD technique to determine the eigenmodes of the system from synthetic data by solving (1) is illustrated in section 3.3. Good agreement between the eigenmodes extracted by the DMD technique and the true eigenmodes is observed.
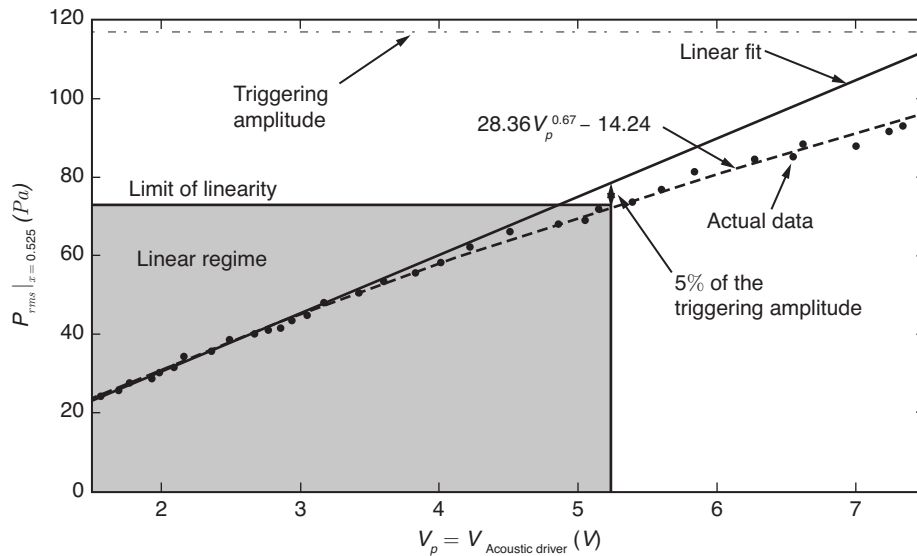
Figure 21: Identification of the linear regime. The acoustic forcing is conducted at 300 Hz with $K = 764$ W and $\dot{m} = 2.34$ g/s. A power law is used to fit the response of the system. The resulting equation for the fit reads $28.36\,V_p^{\,0.67} - 14.24$. The shaded area indicates the linear regime.

Applying the DMD technique to experimental data warrants an estimation of robustness of the DMD algorithm in the presence of noise and of the uncertainty in the relevant output quantities.

As a first step, the noise in the system has to be characterized. Figure 22 presents an estimate of the noise level in the system. The noise levels measured at locations $x = 0.1$ and $x = 0.8$ are shown in figures 22(a, c). The input waveforms at the same locations, used to perform DMD, are shown in figures 22(b, d). These waveforms are mostly aligned with the second eigenmode of the system. The horizontal line indicates the rms-level of the corresponding signal which is used to measure the signal strength. The noise level is then estimated as the ratio of the rms-level of the noise to the rms-level of the signal at the locations of the microphones. The resulting noise-level data, plotted along the duct, is shown in figure 22(e). The maximum noise level is determined as 4.2% and occurs at $x = 0.525$. Since the second eigenmode of the system is excited, the above location is close to the acoustic pressure node and hence has the highest relative noise level. Similarly, the relative noise level is determined for computing the first eigenmode (see figure 22f).

The power supplied to the heater in our case is $K = 747\,W$, which is in the subcritical transition zone (see figure 12). The rms-amplitude of the signals in figure 22(b, d) are smaller than the rms-amplitude (87 Pa) of the linearity limit. Since the experiment is performed for lower values of K, acoustic pressure data with a larger signal-to-noise ratio can be used as the amplitude of the linearity limit is higher. In the present experiments, the maximum value of K used is 747 W (figure 13). Hence, the maximum noise level encountered in the determination of eigenmodes of the system is 4.2%.
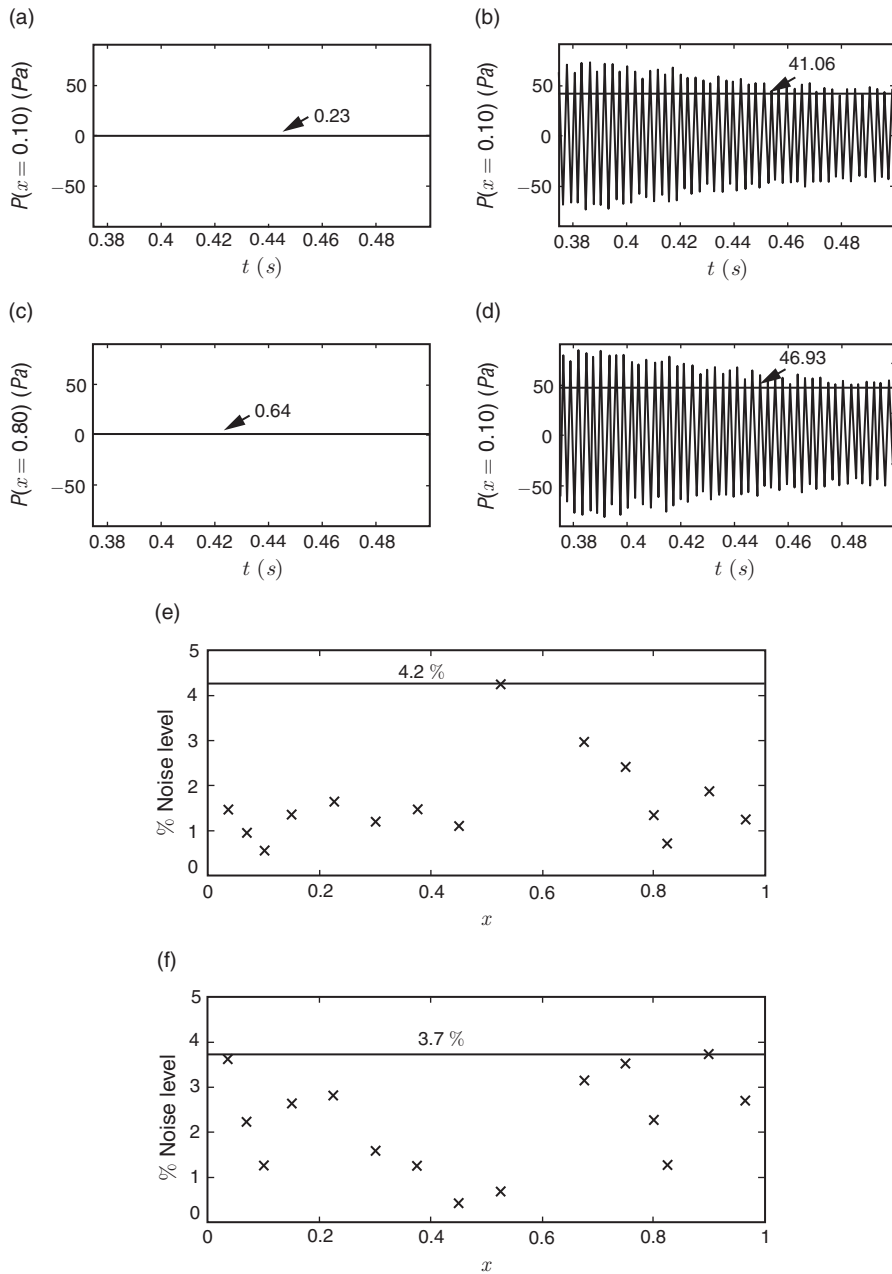
Figure 22:   Estimation of noise levels encountered in the experiments. (*a*) and (*c*) noise levels measured at locations $x = 0.10$ and $x = 0.80$. (*b*) and (*d*) the input waveform measured at the same locations, used to perform DMD. The horizontal line indicates the rms-level of the corresponding signal. The relative noise level is estimated as the ratio of the rms-level of the noise to the rms-level of the signal at the microphone locations. Results are shown for determining the (*e*) second and (*f*) first eigenmode of the system. The remaining parameters are $\dot{m} = 2.34\ g/s$ and $K = 747\ W$.

The uncertainty in the inner product $|{<}p_i,\ p_j{>}|$, which determines the non-orthogonality of the eigenmodes, is determined as follows. For a conservative estimate, noise at levels shown in figures 22*e* and *f* is added numerically to the data set obtained from the experiments before the DMD is performed. The data provided to the DMD are first projected onto the proper orthogonal decomposition (POD) modes to reduce the effect of noise [47] in the determination of the eigenmodes. A lower cut-off is defined on the number of POD modes (based on their energy content) to be used for the projection [23]. In our case, the cut-off is set as 10 for the application of DMD on the downstream side of the heater, while no such cut-off is set for the upstream side. Several numerical realizations (in the present case, 200) are performed and the values of $|{<}p_i,\ p_j{>}|$ are recorded.

The obtained values of $|{<}p_i,\ p_j{>}|$ are distributed over 20 bins of size 2×10^{-3} for the data range $0.114 - 0.134$. Figure 23*a* shows the histogram for the above realizations. The histogram is then normalized by the total number of realizations to
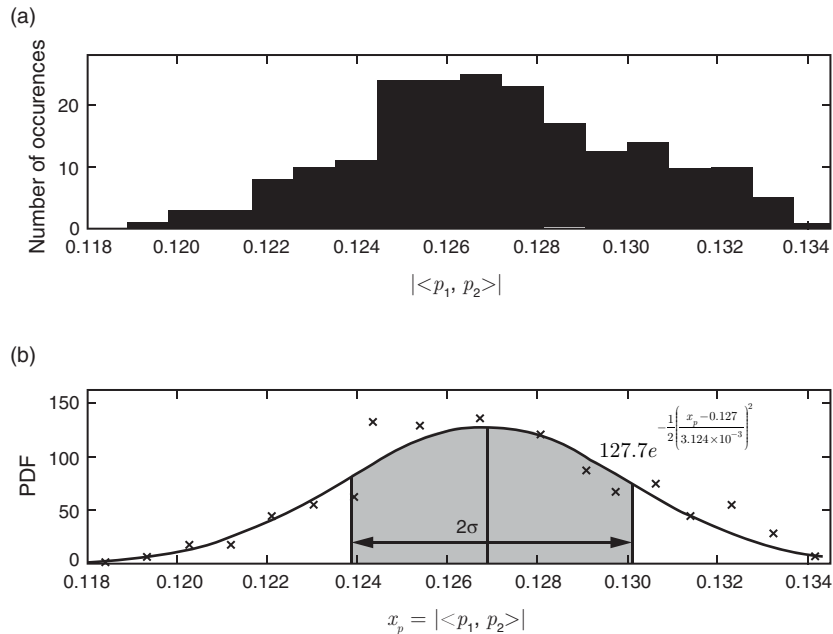
(a)

(b)

Figure 23: Illustratation of the robustness of the DMD algorithm in the presence of noise. (*a*) Histogram plot based on 20 bins for the value of the inner product $|{<}p_i,\ p_j{>}|$ from 200 realizations with random noise added to the experimental data. The added noise level is equivalent to the one shown in figure 22*e, f*. (*b*) Probability density function (PDF) for the above histogram. The cross symbols indicate the histogram data, and the continuous line indicates a Gaussian distribution fit. The equation of the fit is also indicated. The mean value x_m of $|{<}p_i,\ p_j{>}|$ is 0.127, and the standard deviation σ is 3.124×10^{-3}. The percentage error associated with $|{<}p_i,\ p_j{>}|$ is evaluated as $\sigma/x_m \times 100 = 2.46$. This value is used as the amplitude of the error bar [46] indicated in figure 13*d*. The governing parameters are the same as in figure 22.

obtain the probability density function (PDF) for $|<p_i, \ p_j>|$, see figure 23b. A normal distribution is fitted to the PDF and, for our example, is of the form $127.7\mathrm{e}^{-((x_\mathrm{p} - 0.127)/3.124 \times 10^{-3})^2/2}$ where x_p represents the stochastic variable $|<p_i, \ p_j>|$. From the above distribution, the mean x_m and standard deviation σ are found to be 0.127 and 3.124×10^{-3} respectively. The relative normalized standard deviation (in percent) is determined as $\sigma/x_m \times 100 = 2.5$ and is used as the percentage amplitude of the error bar [46] indicated in figure 13(d). The above spread in the value of $|<p_i, \ p_j>|$ is indicated as shaded region in figure 23(b).

REFERENCES

[1]   P. L. Rijke. The vibration of the air in a tube open at both ends. *Philosophical Magazine*, 17:419–422, 1859.

[2]   Y. P. Kwon and B. H. Lee. Stability of the Rijke thermoacoustic oscillation. *J. Acoust. Soc. Am.*, 78:1414–1420, 1985.

[3]   C. C. Hantschk and D. Vortmeyer. Numerical simulation of self-excited thermoacoustic instabilities in a Rijke tube. *Journal of Sound and Vibration*, 227:511–522, 1999.

[4]   P. Subramanian, S. Mariappan, P. Wahi, and R. I. Sujith. Bifurcation analysis of thermoacoustic instability in a horizontal Rijke tube. *International journal of spray and combustion dynamics*, 2:325356, 2010.

[5]   S. Mariappan and R. I. Sujith. Modeling nonlinear thermoacoustic instability in an electrically heated Rijke tube. *Journal of Fluid Mechanics*, 680, 511-533, 2011.

[6]   Taraneh Sayadi, Vincent Le Chenadec, Peter J. Schmid, Franck Richecoeur, and Marc Massot. Thermoacoustic instability - a dynamical system and time domain analysis. *Journal of Fluid Mechanics*, 753:448–471, 8 2014.

[7]   K. I. Matveev. *Thermo-acoustic instabilities in the Rijke tube: Experiments and modeling*. PhD thesis, California Institute of Technology, Pasadena, 2003.

[8]   W. S. Song, S. Lee, D. S. Shin, and Y. Na. Thermoacoustic instability in the horizontal Rijke tube. *Journal of Mechanical Science and Technology*, 20:905–913, 2006.

[9]   K. Balasubramanian and R. I. Sujith. Non-normality and nonlinearity in combustion acoustic interaction in diffusion flames. *Journal of Fluid Mechanics*, 594:29–57, 2008.

[10] K. Balasubramanian and R. I. Sujith. Thermoacoustic instability in a Rijke tube: Non-normality and nonlinearity. *Phy. Fluids*, 20:044103, 2008.

[11] P. J. Schmid and D. S. Henningson. *Stability and Transition in Shear Flows*. Springer-Verlag, New York, 2001.

[12] S. Mariappan and R. I. Sujith. Thermoacoustic instability in solid rocket motor - non-normality and nonlinear instabilities. *Journal of Fluid Mechanics*, 653:1–33, 2010.

[13] M. P. Juniper. Triggering in the horizontal Rijke tube: Non-normality, transient growth and bypass transition. *Journal of Fluid Mechanics,* 667:272–308, 2011.

[14] I. Waugh, M. Geu, and M. Juniper. Triggering, bypass transition and the effect of noise on a linearly stable thermoacoustic system. *Proceedings of the Combustion Institute*, 33(2):2945–2952, 2011.

[15] I. C. Waugh and M. Juniper. Triggering in a thermoacoustic system with stochastic noise. *International Journal of Spray and Combustion Dynamics*, 3:224–242, 2011.

[16] P. J. Schmid. Nonmodal stability theory. *Annual Review of Fluid Mechanics*, 39(1):129–162, 2007.

[17] D. S. Henningson and S. Reddy. On the role of linear mechanisms in transition to turbulence. *Phy. Fluids*, 6:1396–1398, 1994.

[18] A. Hanifi, P. J. Schmid, and D. S. Henningson. Transient growth in compressible boundary layer flow. *Physics of Fluids*, 8(3):826–837, 1996.

[19] E. W. Mayer and E. Reshotko. Evidence for transient disturbance growth in a 1961 pipe flow experiment. *Phy. Fluids*, 9:242–244, 1997.

[20] M. Matsubara and P. H. Alfredsson. Disturbance growth in boundary layers subjected to free-stream turbulence. *Journal of Fluid Mechanics*, 430:149–168, 2001.

[21] J. H. M. Fransson, L. Brandt, A. Talamelli, and C. Cossu. Experimental and theoretical investigation of the nonmodal growth of steady streaks in a flat plate boundary layer. *Phy. Fluids*, 16:3627–3638, 2004.

[22] J. H. M. Fransson, A. Talamelli, L. Brandt, and C. Cossu. Delaying transition to turbulence by a passive mechanism. *Phys. Rev. Lett.*, 96(6):064501, Feb 2006.

[23] P. J. Schmid. Dynamic mode decomposition of numerical and experimental data. *Journal of Fluid Mechanics*, 656:5–28, 2010.

[24] K. I. Matveev and F. E. C. Culick. A study of the transition to instability in a rijke tube with axial temperature gradient. *Journal of Sound and Vibration*, 264(3): 689–706, 2003.

[25] V. Bellucci, B. Schuermans, D. Nowak, P. Flohr, and C. O. Paschereit. Thermoacoustic modeling of a gas turbine combustor equipped with acoustic dampers. *Proceedings of ASME Turbo Expo, Power for Land, Sea, and Air*, pages GT2004–53977, 2004.

[26] B. Schuermans, H. Luebcke, D. Bajusz, and P. Flohr. Thermoacoustic analysis of gas turbine combustion systems using unsteady CFD. *Proceedings of ASME Turbo Expo, Power for Land, Sea, and Air*, pages GT2005–68393, 2005.

[27] S. M. R. Hosseini and C. J. Lawn. Non-linearities in the thermo-acoustic response of a premixed swirl burner. *Twelfth International Congress on Sound and Vibration,* pages 11–14 July, Lisbon, 2005.

[28] C. W. Rowley, I. Mezic, S. Bagheri, P. Schlatter, and D. S. Henningson. Spectral analysis of nonlinear flows. *Journal of Fluid Mechanics*, 641:115–127, 2009.

[29] P. J. Schmid, K. E. Meyer, and O. Pust. Dynamic mode decomposition and proper orthogonal decomposition of flow in a lid-driven cylindrical cavity. In *8th International Symposium on Particle Image Velocimetry*, Melbourne, Australia, August 25-28 2009.

[30] P. J. Schmid, L. Li, M. P. Juniper, and O. Pust. Applications of the dynamic mode decomposition. *Theor. Comput. Fluid Dyn.*, 641, 2010.

[31] P. J. Schmid. Application of the dynamic mode decomposition to experimental data. *Experiments in Fluids*, pages 1–8, 2011.

[32] S. Mariappan, R. I. Sujith, and P. J. Schmid. Experimental investigation of non-normality of thermoacoustic interaction in an electrically heated Rijke tube. In *47th AIAA/ASME/SAE/ASEE Joint Propulsion Conference*, San Diego, California, July 31 - August 3 2011. AIAA 2011 - 5555.

[33] F. E. C. Culick. Unsteady motions in combustion chambers for propulsion systems. Technical Report AG-AVT-039, RTO AGARDorgraph, 2006.

[34] F. Nicoud, L. Benoit, C. Sensiau, and T. Poinsot. Acoustic modes in combustors with complex impedances and multidimensional active ames. *AIAA Journal*, 45:426–441, 2007.

[35] T. Poinsot and D. Veynante. *Theoretical and numerical combustion*. R.T. Edwards, Inc., Philadelphia, second edition, 2005.

[36] L. Crocco. Theory of combustion instability in liquid propellant rocket motors. Technical Report 0429886, RTO AGARDorgraph, 1956.

[37] M. J. Lighthill. The response of laminar skin friction and heat transfer to fluctuations in the stream velocity. *Proceedings of the Royal Society of London. Series A, Mathematical and Physical Sciences*, 224(1156):1–23, 1954.

[38] L. E. Kinsler, A. R. Frey, A. B. Coppens, and J. V. Sanders. *Fundamentals of Acoustics*. John Wiley & Sons, Inc., USA, 4 edition, 2000.

[39] Frederick W. King. *Hilbert Transforms*. Cambridge University Press, 2009.

[40] S. H. Strogatz. *Nonlinear Dynamics and Chaos: with applications to Physics, Biology, Chemistry, and Engineering*. Westview Press, Colorado, first edition, 2000.

[41] R. I. Sujith, G. A. Waldherr, and B. T. Zinn. An exact solution for one-dimensional acoustic fields in ducts with an axial temperature gradient. *Journal of Sound and Vibration*, 184(3):389–402, 1995.

[42] B. D. Bellows. *Characterization of Nonlinear Heat Release-Acoustic Interactions In Gas Turbine Combustors*. PhD thesis, Georgia Institute of Technology, Atlanda, 2006.

[43] M. Abom and H. Boden. Error analysis of two-microphone measurements in ducts with flow. The *Journal of the Acoustical Society of America*, 83(6):2429–2438, 1988.

[44] S. Nagaraja, K. Kedia, and R.I. Sujith. Characterizing energy growth during combustion instabilities: Singularvalues or eigenvalues? *Proceedings of the Combustion Institute*, 32(2):293–2940, 2009.

[45] S. W. Rienstra and A. Hirschberg. An introduction to acoustics. *Intl. journal of spray and combustion dynamics*, pages IWDE 92–06, 2008.

[46] J. P. Holman. *Experimental methods for Engineers*. McGraw-Hill, Inc., USA, 6 edition, 1994.

[47] D. C. Negrete, D. A. Spong, and S. P. Hirshman. Proper orthogonal decomposition methods for noise reduction in particle-based transport calculations. *Phy. Plasmas*, 15:092308, 2008.